Implementation of a Raman Sideband Cooling for ^{87}Rb

Bachelorarbeit von
Christoph Braun
05.10.2015

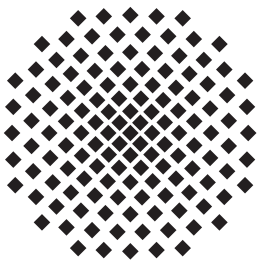

Universität Stuttgart
5. Physikalisches Institut

Prof. Dr. Tilman Pfau
Dr. Sebastian Hofferberth

Implementierung einer Raman Seitenband Hühlung für ^{87}Rb

Zusammenfassung Im Rahmen dieser Arbeit wurde ein Aufbau realisiert um Atome selbst bei hohen Dichten weiter effizient kühlen zu können. Das entartete Raman Seitenband Kühlen ermöglicht höhere Dichten und niedrigere Temperaturen als die Kühlung mittels magneto-optischer Falle sowie folgender optischer Molasse und Kompression. Darüber hinaus bestünde die Möglichkeit Atome innerhalb einer optischen Dipolfalle zu kühlen jedoch wird beim Raman Seitenband Kühlen gegenüber dem Verdampfungskühlen die Atomzahl weniger reduziert.

In der vorliegenden Arbeit wird zunächst die grundlegende Struktur der atomaren Energieniveaus erläutert, daraufhin werden die grundlegenden Elemente des Aufbaus beschrieben sowie die Intensitätsstabilisierung näher charakterisiert. Der grundsätzliche Ablauf eines Kühlzyklus auf atomarer Ebene wird erklärt und später die Kopplung zwischen den magnetischen Hyperfeinstrtukturniveaus diskutiert. Die erwartbare Leistungsfähigkeit des gesamten Prozesses wird gemeinsam mit den ersten Messungen im Zusammenhang mit dieser Kühlmethode vorgestellt.

Implementation of a Raman Sideband Cooling for ^{87}Rb

Abstract In the Course of this thesis a setup which theoretically enables efficient cooling even at high densities has been realized. Degenerate Raman sideband cooling makes it possible to cool to lower temperatures and higher densities than achievable with common magneto-optical trapping and subsequent optical molasses and compression. Furthermore this cooling process could be implemented inside an optical dipole trap where cooling with less loss of trapped atoms could be achieved in comparison to evaporative cooling.

In the presented thesis the basic structure of atomic energy levels is illustrated, next the basic elements of the setup are described and the characteristics of the intensity stabilization are specified. The process of cooling is explained on the single atom level together with the origin of the coupling between different magnetic hyperfine levels. The expectable performance is discussed along with the first measurements conducted in connection with Raman sideband cooling.

Declaration

I hereby declare that this submission is my own work and that, to the best of my knowledge and belief, it contains no material previously published or written by another person, except where due acknowledgment has been made in the text.

Christoph Braun
Stuttgart, October 5, 2015

Contents

1. The Rubidium Atom

1.1. Atomic Structure

The Rubidium Atom is one of the alkali metals. The alkali atoms lying in the first group of the periodic table all have in common that their outermost electron is in an s-orbital. The beneficial thing about that is that the inner electrons in the closed shells do not contribute to the total spin and angular momentum, therefore the quantum mechanical description of the hydrogen atom can be adapted. As there is obviously more than one electron one has to consider the electron-electron and electron-nucleus interaction in the Hamiltonian. A simple approach just assumes that the inner electrons sort of shield the nucleus' core resulting in a single charged core and an electron. The result would be the binding energies of the hydrogen atom, as this is not true one can modify the principal quantum number n depending on the outer electron's orbital. This correction is known as quantum defect [Foot, 2005]. With the assumptions discussed one can calculate the spin-orbit interaction and the ongoing hyperfine structure arising from the nuclear spin interacting with the electron spin and orbit.

1.2. Fine-structure

In 1922 Stern and Gerlach discovered the electron spin due to its interaction with magnetic fields [Gerlach and Stern, 1922]. An electron orbiting a nucleus could in principle also be considered as a current resulting in a magnetic field with which the electron spin could interact. Following this consideration the angular momentum - embodying the orbital movement - should give rise to an energy difference in the atomic energy structure. As the angular momentum of an electron does contribute to the energy levels of the atom, the arising energy difference is called fine-structure splitting. The Hamiltonian results from the Lorentz transformation for electromagnetic fields or in a more complex from the Dirac equation. In a "classical" approach the electron sees the electric field of the core resulting in a magnetic field which is coupling to the electron's spin, resulting in the following Hamiltonian in spherical coordinates,

$$H_{FS} = -\hat{\vec{\mu}}_s \cdot \vec{B} = \frac{\mu_B g_s \partial_r V(r)}{mc^2 \hbar e r} \hat{\vec{L}} \cdot \hat{\vec{S}}. \tag{1}$$

Here μ_B is the Bohr magneton, g_s the electron spin g-factor, m the electron's rest mass, c the speed of light and e the elementary charge. Due to the transformation back to the laboratory frame arises a term, the so called Thomas precession [Jackson, 1982]

$$H_T = -\frac{\mu_B \partial_r V(r)}{mc^2 \hbar e r} \hat{\vec{L}} \cdot \hat{\vec{S}}. \tag{2}$$

The single angular momentum operators $\hat{\vec{L}}$ and $\hat{\vec{S}}$ are now coupled and result in new quantum numbers $\hat{\vec{J}}$ and m_J, the composed angular momentum. Note that the basis of $\hat{\vec{L}}$ and $\hat{\vec{S}}$ does not lose its validity but the projection of the angular momentum operator, e.g. $\hat{L}_z$ (quantization axis along z), is no longer diagonal in this basis, therefore it's convenient to change the basis and introduce new operators. Consequently the total energy shift caused by the spin-orbit interaction is

$$\begin{gathered} \Delta E_{\mathrm{FS}} \langle n,L,S,J,m_J | H_{FS} + H_T | n,L,S,J,m_J \rangle = \\ \frac{\mu_B (g_s - 1) \langle n | \partial_r V(r) | n \rangle}{mc^2 \hbar e r} [J(J+1) - L(L+1) - S(S+1)]. \end{gathered} \tag{3}$$

1.3. Hyperfine-structure

The nuclear spin's $\hat{\vec{I}}$ magnetic moment is given by

$$\vec{\mu}_\mathrm{I} = g_I \mu_N \hat{\vec{I}}, \tag{4}$$

it interacts in a similar way with a magnetic field arising from the interaction of the core with the electron's spin and orbit. The derivation follows analogous, with some more terms. The resulting angular momentum $\hat{\vec{I}}$ and therefore also m_F is composed from $\hat{\vec{J}}$ and $\hat{\vec{I}}$. The energy shift [Steck, 2001], if only the magnetic dipole moment is taken into account, reads

$$\Delta E_\mathrm{HFS} = \frac{1}{2}\mathrm{A_{HFS}}[F(F+1) - I(I+1) - J(J+1)], \tag{5}$$

where $\mathrm{A_{HFS}}$ is called hyperfine-structure constant, which also depends on the atoms state. To give a rough example for ^{87}Rb in $5^2\mathrm{S}_{1/2}$ the hyperfine-structure constant is $\mathrm{A_{HFS}} = h \cdot 3.417\,\mathrm{GHz}$ [Steck, 2001].

1.4. Zeeman Effect

As described above, the atom's electron(s) interact with electromagnetic fields. If a magnetic field is applied the Hamilton-operator is composed by

$$H_B = \frac{\mu_B}{\hbar}(g_s \hat{\vec{S}} + g_I \hat{\vec{I}} + g_L \hat{\vec{L}}) \cdot \mathbf{B}. \tag{6}$$

In general the resulting Hamiltonian $H_{HFS} + H_B$ needs to be calculated and diagonalized to find the resulting energy shift, often one does not find an analytical solution so the calculation needs to be done numerically. For a state with $J = 1/2$, e.g. the Rb groundstate, the Breit-Rabi formula can be obtained, the direction of the magnetic field defines the quantization axis then, preferably z.

$$\begin{aligned}\Delta E_{|J=1/2,m_J,m_I\rangle} &= -\frac{\mathrm{A_{HFS}}(I+1/2)}{2(2I+1)} + \mu_B g_I \left(m_I + \frac{1}{2}\right) B \\ &\pm \frac{\mathrm{A_{HFS}}(I+1/2)}{2}\left[1 + 2\frac{\mu_B(g_J - g_I)B}{\mathrm{A_{HFS}}(I+1/2)}\frac{2m_I+1}{2I+1} + \left(\frac{\mu_B(g_J-g_I)B}{\mathrm{A_{HFS}}(I+1/2)}\right)^2\right]^{1/2}\end{aligned} \tag{7}$$

$$g_J = 1 + \frac{J(J+1) - L(L+1) + S(S+1)}{2J(J+1)} \tag{8}$$

$$g_{I,^{87}\mathrm{Rb}} = -0.000995 \tag{9}$$

$$\tag{10}$$

2. Setup

2.1. Lattice Laser

Our setup (cf. Fig. 1) for Raman sideband cooling consists of a red-detuned optical lattice derived from a `TOPTICA TA pro`, beat note locked to a reference laser. The lattice laser is locked resonant to the Rb^{87} $F = 2 \rightarrow F' = 2$ transition of the D_2-line. The reference laser is locked to an ultra-stable cavity, the reference laser's locking setup is described in [Tresp, 2013]. The beat note lock technique utilizes the beat of two overlapped interfering lasers. Adding two sinusoidal waves the resulting intensity, which is proportional to the time averaged square of the electric field, then reads

$$\begin{aligned} I(t) &\propto (E_1 \sin(\omega_1 t) + E_2 \sin(\omega_2 t))^2 \\ &\propto \frac{E_1^2}{2}(1 - \cos(2\omega_1 t)) + \frac{E_2^2}{2}(1 - \cos(2\omega_2 t)) + \frac{E_1 E_2}{2}\left(\cos((\omega_1+\omega_2)t) + \cos((\omega_1-\omega_2)t)\right). \end{aligned} \tag{11}$$

The result is, among other terms, a sum of terms of the sum and difference frequency of the two waves. Optical frequencies are in the range of 10^{14} Hz and electronics aren't yet able to resolve changes in on that timescale, therefore the only change in intensity which is detected by a biased `Hamamatsu G4176-03` photodiode arises from the difference frequency term. This signal is then amplified and applied to the input of an `Analog Devices EVAL-ADF4007EB1` evaluation board. Inside this evaluation board the input signal's frequency is divided by a variable factor $N = 8, 16, 32, 64$ and compared to a reference signal whose frequency is divided by two by default. These two signals are transformed into digital pulses which are then compared with respect to their phase. The result of this operation is then fed into a charge-pump which creates a signal in the range of 0 V to 3 V depending on the phase difference, a similar setup is described in [Appel *et al.*, 2009]. The resulting signal is then fed to a PID-controller, which operates in three different stages. A PID-controller is used to stabilize a signal to a desired value, where it utilizes different frequency regimes of the input signal, to derive an output signal affecting the input signal. The electronic schematic is depicted in Fig. 18, the capacitor in the integral-part was changed to $C_I = 10\,\mu$F.

- **P-part:** The proportional part creates a signal, which corresponds to the instantaneous deviation of the input signal from the ideal value. This part of the controller corresponds to the higher frequency components of the signal.

- **I-part:** The integration part of the controller can be considered to sum up all the deviations from the ideal value overtime, e.g. if the signal is constant but higher than the desired value the arising error signal would rise to infinity (with some limits given by the electronics). Since e.g. very fast oscillations would average out on this part one can use a low-pass filter before handing the signal to the integrator, the resulting error signal therefore reacts on timescales longer than the P-part. It also corresponds to the history of the signal.

- **D-part:** The derivative part utilizes the current change of the signal to derive a error signal. The error signal is proportional to the derivative of the signal, it tries to minimize the drift towards a value. The derivative is not affected by the current value, therefore a simple D-part cannot work as a controller on its own.

Note that the term proportional to the deviation is ambiguous as it leads to an error signal, which tries to push or pull the input signal's value to the ideal value, e.g. if the signal is too high the error signal could have both signs, the important points is that it leads to a process which tries to reduce the input signal. The input signal to the PID-controller is processed such that the error signal is zero if the frequency of the laser corresponds to the desired frequency. The error-signal is fed to the laser's current-controller as well as the piezo-controller to stabilize the lasers frequency. Since these two laser components correspond to corrections on different timescales the output signal is split into lower and higher frequency components which are fed into the piezo and current control. The resulting beat note signal between the reference laser and the lattice laser in the frequency domain is depicted in Fig. 2

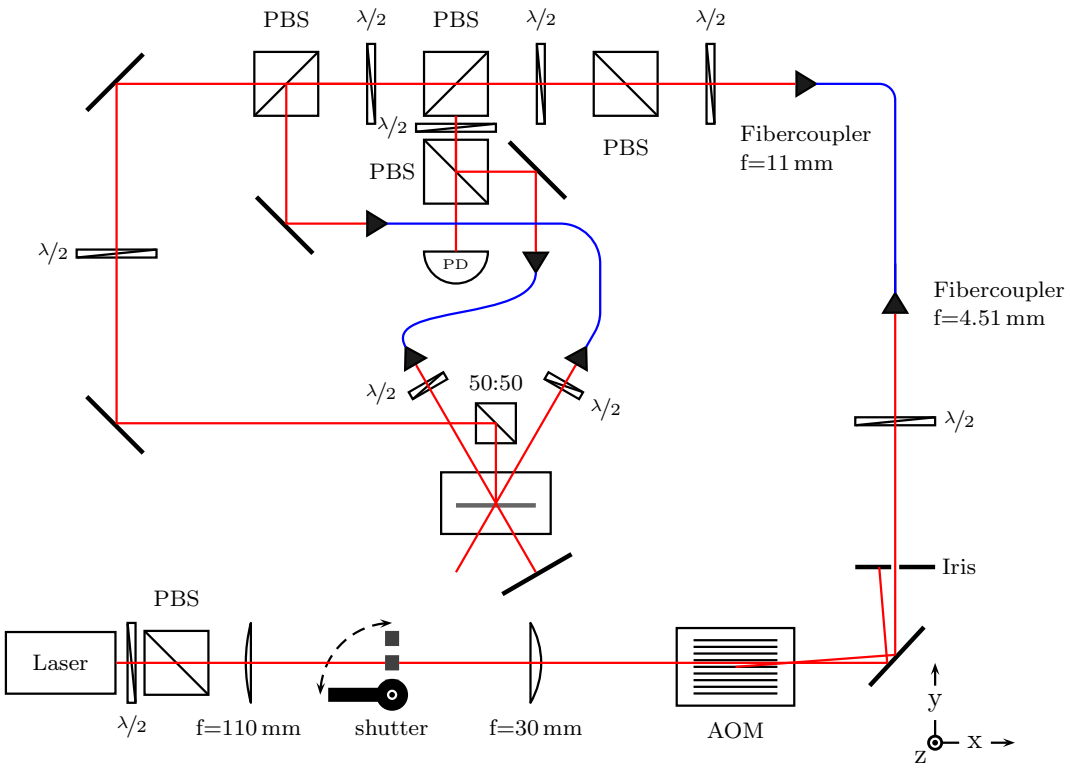

Fig. 1: The Setup. The main part of the setup for Raman sideband cooling consists of the three interfering beams the two horizontal beams subtend an absolute angle $\alpha = \frac{55}{2}\,^\circ$ with respect to the y-axis. To create a standing wave one beam is retroreflected, the vertical beam enters the vacuum chamber from below. The pump beam propagates along -z-direction. The red lines correspond to propagating laser beam, the blue lines are polarization-maintaining fibers.

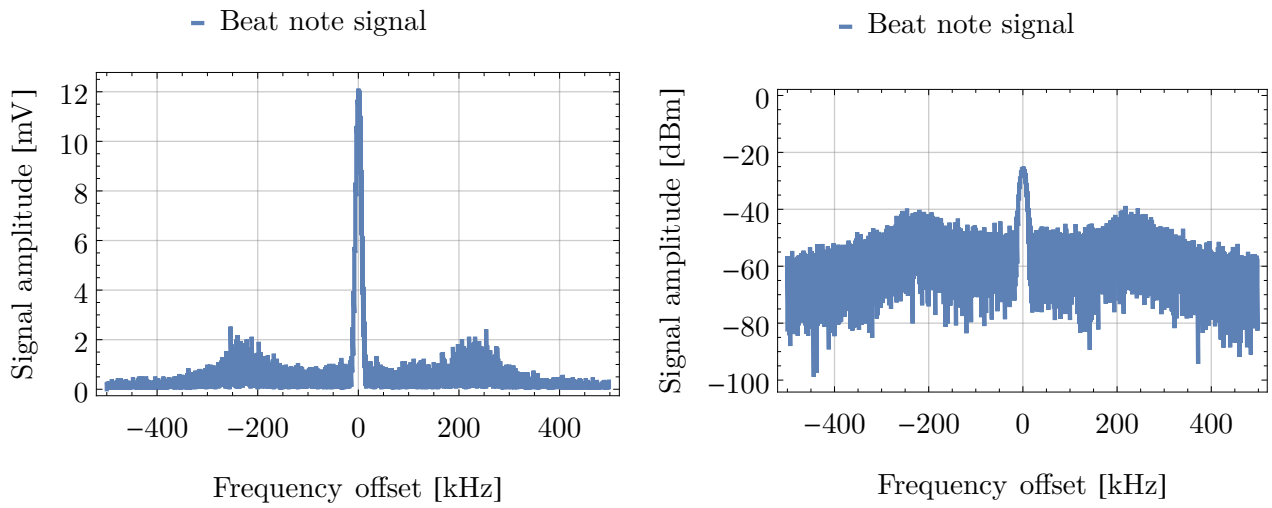

Fig. 2: Beat note signal between locked and reference laser. (**Left**) Beat note signal in the frequency domain with a linear voltage axis. The beat shows a distinct peak with a line width in the kHz range. (**Right**) The beat note signal with the voltage depicted in dBm.

2.2. Raman-Pump Laser

The Laser to pump the atoms to a given magnetic hyperfine level is stabilized in a similar manner. The `Vitawave Extended Cavity Diode Laser` is also beat note locked but to the $F = 1 \rightarrow F' = 0$ transition of the D_2-line. This laser is also used during the magneto-optical trapping (MOT) to repump the atoms from $F = 1$ to $F = 2$. The light for Raman sideband cooling and for the MOT-phase does not take the same optical path to the experiment and the is therefore is split by two acousto-optic modulators (AOM). The first AOM diffracts the light during the MOT phase into the first order maximum, the zeroth order is reflected by a D-shaped mirror to the second AOM which is used to adjust the power in the Raman-pump beam during the Raman sideband cooling phase. The frequency is adjusted for both phases individually. After the MOT phase, the laser is jumped to the red. The beam in the chamber has an $1/e^2$-radius of 1.1 mm and provides up to 2 mW of power.

2.3. Lattice Optics and Intensity Stabilization

The lattice depth and curvature depend on the light's local intensity (cf. subsection 4.1), due to that the local intensity in the lattice has to be as constant as possible. The local intensity is made up of two things first the intensity itself and second the polarization, if either changes, the potential and the oscillation frequency in the trap will change. To achieve a stable lattice the intensity and polarization has to be as stable as possible, to do so polarization fluctuations are translated into intensity fluctuations and then the intensity is stabilized.

2.3.1. Intensity Stabilization Electronics

The depicted setup in Fig. 1 adjusts the intensity via an AOM in front of the first fiber. The radio frequency's power is determined by a control loop, which starts by measuring the intensity with a logarithmic photodiode. Using such a logarithmic photodiode provides provides a good signal to noise ratio over some orders of magnitude so that the lattice can be ramped down while the intensity is still controlled. A fit was conducted in order to quantify the response of the logarithmic photodiode, it is depicted in Fig. 3. The output voltage depending on the input is depicted in Fig. 3, as well as the frequency response. It was measured modulating the AOM power sinusoidal, but due to the

nonlinear response function of the AOM the sinusoidal signal got distorted, therefore the frequency response does not perfectly represent the response to a sinusoidal input. Yet there was a modulation because the AOM power was modulated from its minimum to half of its maximum. The measured frequency response corresponds to the complete system made up of the AOM and the logarithmic photodiode.

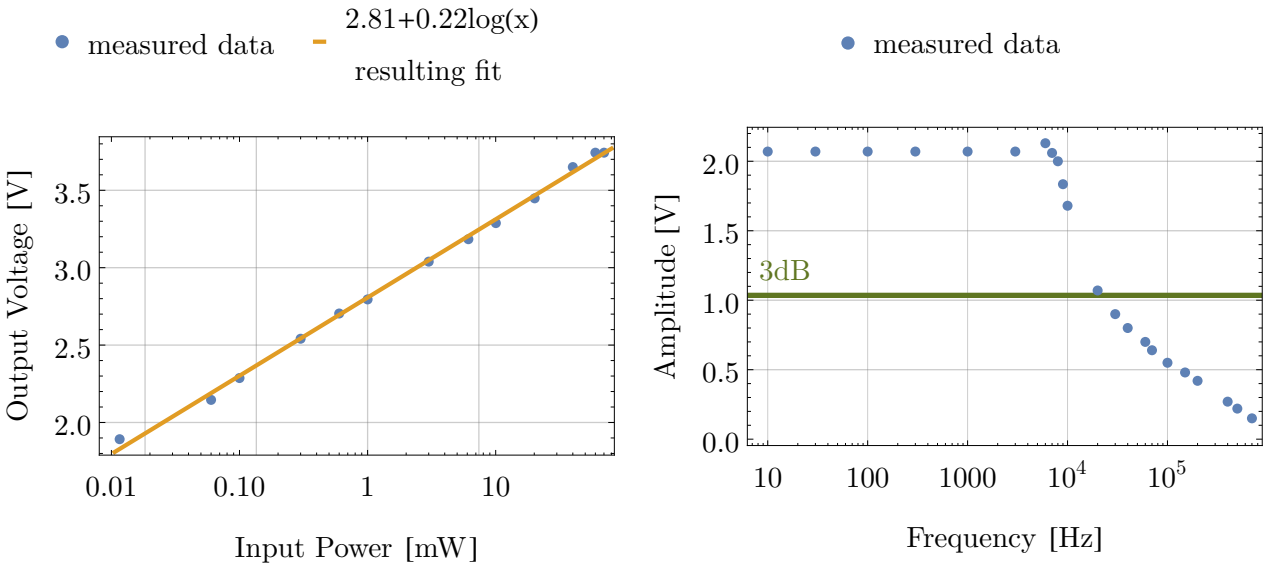

Fig. 3: Power and frequency response. (**Left**) Power dependent output voltage of the logarithmic photodiode. The photodiode does not get saturated in the range used for intensity and polarization stabilization. (**Right**) The logarithmic photodiode's frequency response. The response function does not show any frequency dependence up to $\approx 5\,\mathrm{kHz}$, afterwards the response decreases for higher frequencies. The 3 dB point corresponds to halving of the incoming power, the quantity effectively mapped her is the output voltage.

In principle the photodiode itself does not react logarithmic to the incoming intensity or power, but an logarithmic amplifier (`Analog Devices AD8307`) translates the linear photodiode's response to a logarithmic one which is used to stabilize the polarization and intensity.

The signal derived from the logarithmic amplifier is then again fed into a PID-controller, where it is internally compared to a reference voltage set by a function generator. The function generator also provides the possibility to dynamically adjust the lattice intensity in order to release the atoms adiabatically (cf. subsection 5.4). The PID-controller's output is then used to again adjust the AOM power, here only the faster part corresponding to higher frequency components is used to stabilize the intensity.

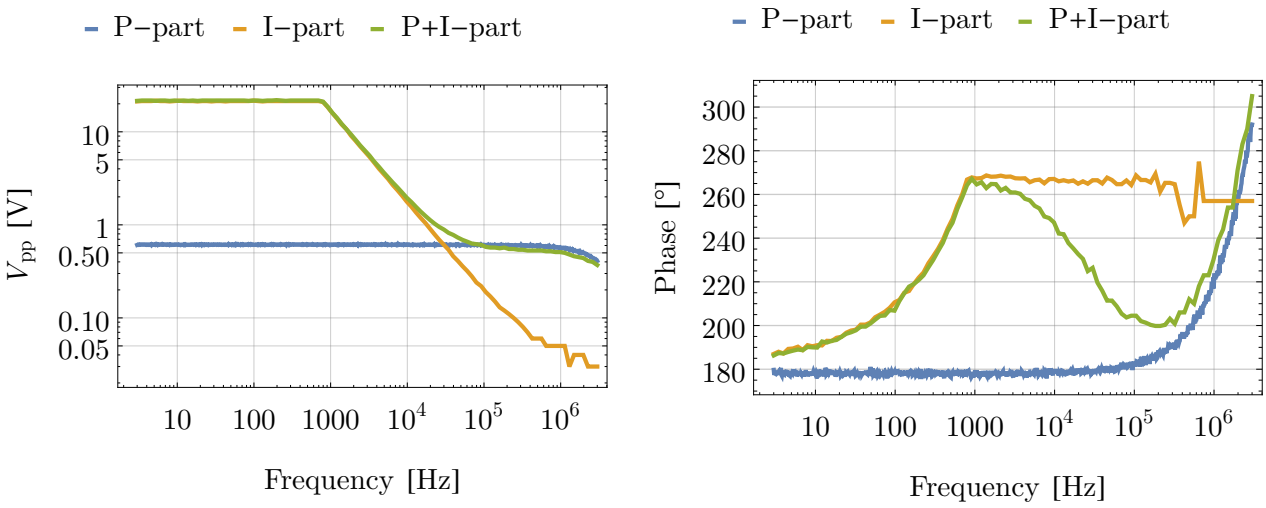

Fig. 4: Amplitude and phase of the PID-controller's output used to stabilize the intensity depending on the signal's frequency.(**Left**) Output in dependence of the frequency. For lower frequencies up to 1 kHz the I-part is fast enough to always saturate the electronics, leading to the maximum peak-to-peak Voltage V_{pp}. For higher frequencies the P-part comes into play leading to non-vanishing amplitude whereas the I-part does not contribute any more. (**Right**) Frequency dependent phase between in- and output of the PID-controller. Both parts individually pick up some phase with increasing frequency. Maybe the phase of both parts together drops because the P-part still has less phase shift and due to the decreasing gain of the I-part the signal is dominated by the p-Part.

The PID-controller's inputs were terminated with 50 Ω (R_1 and R_{43} in Fig. 18), the capacitor in the integral part was tested more in-depth because it is an essential part determining the performance of the final stabilization. As the intensity should be stable on a timescale of 1 μs, the integral part of the PID-controller was first tested using a 50 pF capacitor. The intensity seemed stable for a constant input of 3.9 V-6.7 V applied to the PID-controller's reference input. For higher reference signals above 6.7 V the error signal increased, below 3.9 V the intensity began to fluctuate. The intensity was measured with a linear photodiode for reference too.

The resistor in the integral part ranges from 1.8 kΩ to 21.4 kΩ. As the tuneability was assumed to be not sufficient, the integration time constant using the 50 pF capacitor was $\leq 1\,\mu$s, the capacitor therefore was changed to achieve an integration time constant ranging from 0.18 μs to 2.14 μs, using a 100 pF capacitor. The configuration was tested applying a square voltage ($4.0 - 4.5$ V, 100 Hz) and measuring the rise time of the resulting error signal, it was $T_{rise} = 132\,\mu$s. The resistor was put to the lowest value possible, so another smaller capacitor was tested. An 68 pF capacitor was tested achieving a rise-time of $T_{rise} = 80\,\mu$s, again the resistor was set to the lowest value. Using a 15 pF capacitor a rise-time of $T_{rise} = 56\,\mu$s could be achieved. The open-loop gain and phase response were measured applying a sinusoidal signal to the PID- controller's input and measuring the resulting output and phase difference between in- and output. The testing was done applying a $U_{in,pp} = 1$ V sinusoidal frequency, the resulting amplitude was measured with an oscilloscope terminated with 50 Ω. The result is depicted in Fig. 4, it is possible that the absolute phase does not meet the reality, e.g. if the real signal is shifted by 180 °, the result is the same as if it was shifted by −180 °. Another point is that depending on the internal settings of the PID-controller, there is an active inverting operational amplifier leading to an additional phase of 180 °. In Fig. 4 it is assumed that the signal already is inverted, therefore the phase at $\nu = 0$ Hz already is $\Delta\varphi = 180\,°$.

2.3.2. Intensity Stabilization and Lattice Optics

The optical lattice potential arises from four interfering beams, in order to create a stable lattice the intensity in each beam should be as stable as possible.

The optics setup is depicted in Fig. 1. The beam coming out of the laser passes a $\lambda/2$-waveplate in front of a polarizing beamsplitter cube (PBS), this configuration is used to adjust the overall power used for the optical lattice potential. Afterwards the beam passes a telescope to adjust the beam size, this happens in a telescope made of a $f = 110\,\mathrm{mm}$ plano-convex and a $f = 30\,\mathrm{mm}$ plano-convex lens. In the focus in between the two lenses an AOM is placed in order to regulate the intensity. Behind the telescope the beam gets reflected, passes a shutter, which blocks the beam when another phase of the experiment is conducted. The zeroth order of the AOM is blocked, the minus first order maximum is then coupled into a polarization-maintaining fiber.

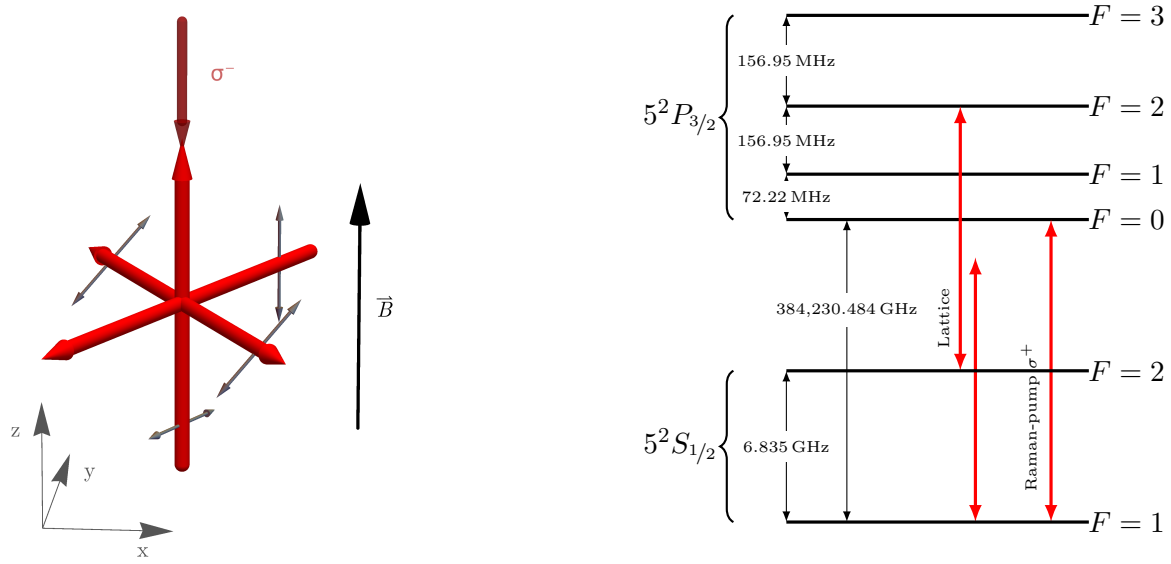

Fig. 5: The polarization and alignment of the beams and their frequencies. (**Left**)Alignment. The coordinate frame is the same as used in all other calculations and descriptions. The brighter red lines correspond to lattice beams, the arrow head indicates the wave vector's direction. The darker red beam is the Raman-pump beam, the polarization is σ^- along the wave vector. The reflected and the transmitted lattice beams subtend an angle of 55 °. The polarizations are depicted in gray. The reflected beams have the same polarization, they subtend an angle of 45 ° with respect to the x-y-plain, the running waves' polarization coincides with the other's wave vector. (**Right**) Frequencies and level scheme. The lattice is resonant to the $F = 2 \rightarrow F' = 2$-transition, it therefore provides a $\approx 6.8\,\mathrm{GHz}$-red-detuned lattice. The Raman-pump beam is resonant to $F = 1 \rightarrow F' = 0$.

The laser power is split by a setup of four subsequent PBS behind the polarization-maintaining fiber. The first PBS (the top right PBS in Fig. 1) is used to filter the polarization behind the polarization-maintaining fiber. After this first PBS a $\lambda/2$-waveplate is used to rotate the polarization in front of the second PBS, which transmits the power for two of the lattice beams and reflects the power for another beam together with the fraction used for stabilization. The latter part then passes another $\lambda/2$-waveplate and hits a PBS, the reflected part is coupled into an polarization maintaining fiber, a small fraction is transmitted through the PBS and hits the logarithmic photodiode, which is used to stabilize the intensity. As previously mentioned the polarization stability is achieved by stabilization of the intensity. Polarization fluctuations are translated into intensity fluctuations by

the first PBS behind the fiber since only the horizontal polarization component passes through. The transmitted beam after the second PBS is then split into two beams of which one is coupled into an polarization-maintaining fiber, the other beam is guided to the chamber in free space, it is reflected twice and then reflected at an 50 : 50-beamsplitter, where half of the power in that beam is lost. A mirror underneath the vacuum chamber redirects the beam upwards. A $\lambda/2$-waveplate is used to align the polarization along the transmitted beam. The beams fed into polarization-maintaining fibers are then collimated by a $f = 11\,\mathrm{mm}$ lens in order to lead to the same beam waist as the beam entering the vacuum chamber. The beam waist directly behind the fiber collimator is $w_0 = 1.1\,\mathrm{mm}$, for each beam the laser provides power of up to 50 mW. The polarization of the beams is adjusted by $\lambda/2$-waveplates behind the fiber collimators. The alignment is shown in Fig. 5.

The two horizontal beams, of which one is retroreflected, cross under 55 °. The polarizations are set such that the two running waves both have the polarization along the other wave's direction of propagation. The standing wave's polarization encloses an angle of 55 ° with respect to the x-y-plain. The Raman-pump beam enters the vacuum chamber from above and is σ^--polarized. But as the magnetic field points in z-direction, which also corresponds to the atoms quantization axis, an atom effectively experiences σ^+ light.

2.4. Additional Elements used in this Experiment

To both cancel stray magnetic fields and apply linear magnetic fields in a certain direction, six coils are mounted around the cuboid vacuum. The coils are approximately rectangular leaving a big area of the vacuum chamber open for optical access. The currents through the coils are driven by `Elektro-Automatik PS 3016-10B`. Each coil has 30 windings and creates an absolute magnetic field per current of 0.95 G/A, 2.15 G/A and 2.30 G/A0 in x-, y- and z-direction. An additional pair of coils is used to create the magnetic quadrupole field during the magneto-optical trapping.

3. Explanation of a Cooling Cycle

3.1. Origin of Sidebands

To understand why a tightly-bound atom can change its motional state by a two-photon Raman transitions we first consider an atom tightly bound in an one dimensional harmonic potential of frequency $\omega_z/(2\pi)$. The atom is addressed by a light field $E \propto \exp(i\vec{k}\cdot\vec{r}) + \exp(-i\vec{k}\cdot\vec{r})$, ignoring the time dependence, the interaction is described by $\langle I,n|\exp(\pm i\vec{k}\cdot\vec{z})|I',n'\rangle$, I represents the atom's internal, n the atoms motional state. The wave vector's projection onto the atom's motion in z-direction is given by $\vec{k}\cdot\vec{z} = |2\pi/\lambda|\cos(\theta)\hat{z} = k_z\hat{z}$, where θ is the angle between the wave vector and the z-axis [Eschner *et al.*, 2003]. The interaction operator here represents the process of absorbing (+) or emitting (-) a photon, the atoms momentum is therefore changed by $\pm\hbar k_z$. Introducing the motional creation and annihilation operators (cf. Equ. 57) the interaction reads $\langle I,n|\exp(\pm ik_z\sqrt{\hbar/(2m\omega_z)}\{a+a^\dagger\})|I',n'\rangle$. If the atoms ground state is much smaller than the wave vector's projection $k_z z_0 = k_z\sqrt{\hbar/(2m\omega_z)} = \eta \ll 1$, the interaction operator can be approximated by

$$\langle I,n|1 \pm i\eta(a+a^\dagger) + O(\eta^2)|I',n'\rangle \approx \delta_{n,n'}\delta_{I,I'} \pm i\eta(\sqrt{n}\,\langle I,n|I',n-1\rangle + \sqrt{n+1}\,\langle I,n|I',n+1\rangle). \quad (12)$$

The approximation is stringently valid if it holds that $\langle\Psi_{motional}|k_z^2 z^2|\Psi_{motional}\rangle^{\frac{1}{2}} \ll 1$ [Wineland *et al.*, 1998], in an harmonic oscillator potential it yields $\eta\sqrt{n+\sqrt{n^2+n}} \ll 1$. This limit is called Lamb Dicke regime, it states that transitions changing the quantum number by more than $\Delta n = 1$ are strongly suppressed. The Lamb Dicke parameter can be rewritten in terms of the recoil energy

$E_{recoil} = \frac{\hbar^2 k_z^2}{2m}$ and the oscillation frequency ω_z, it reads

$$\eta = \sqrt{\frac{\hbar k_z^2}{2m\omega_z}} = \sqrt{\frac{E_{recoil}}{\hbar\omega_z}}. \tag{13}$$

In other words - transitions changing the motional quantum number by more than one are strongly suppressed if the harmonic oscillator's level spacing is large compared to the kinetic energy an atom gains if it hits a single photon. This energy is called recoil energy E_{recoil}. Depending on the Lamb Dicke parameter even transitions changing the motional quantum number by one can be suppressed.

We have now seen that a tightly bound atom can only change its motional quantum number by one, therefore each internal state is dressed by a multiplet of motional states. It is assumed, that the internal excited state is trapped in the same manner. Assuming two states $|g\rangle$ and $|e\rangle$ with energy difference $\hbar\omega_0$, and a dipole allowed transition, then the atom's quantum state can change from the excited state $|e\rangle$ with motional quantum number n to the internal ground state $|g\rangle$ but the motional quantum number can change by zero or one to $n, n+1$ and $n-1$. The energy difference and therefore the photon energy can then be $\hbar\omega_0, \hbar(\omega_0 - \omega_z)$ and $\hbar(\omega_0 + \omega_z)$ for the transitions stated before. Therefore the central transition now shows blue and red sidebands at $\omega_0 \pm \omega_z$. The motional sidebands can only be resolved if the linewidth of the transition between the ground and excited state is smaller than the oscillation frequency.

3.2. The Cooling Process

The atom can be cooled in the system described above, by stimulating the atom on the red sideband $\omega_0 - \omega_z$. The atom then loses one quantum of kinetic energy on average if the motional quantum number doesn't change on average during spontaneous emission.

The setup described above is used to implement another technique to achieve a sample of atoms cooled to the 3D-motional ground state of an optical lattice. The method has been explored in an three-dimensional optical lattice by [Kerman *et al.*, 2000] and [Treutlein *et al.*, 2001]. Previously Raman sideband cooling had been demonstrated in one- and two-dimensional optical lattices [Vuletić *et al.*, 1998; Hamann *et al.*, 1998]. To understand the mechanism of cooling we at first consider the simple case, in which the optical potential for all three $|F = 1, m_F\rangle$ magnetic hyperfine levels is identical. We than have the situation depicted in Fig. 6.

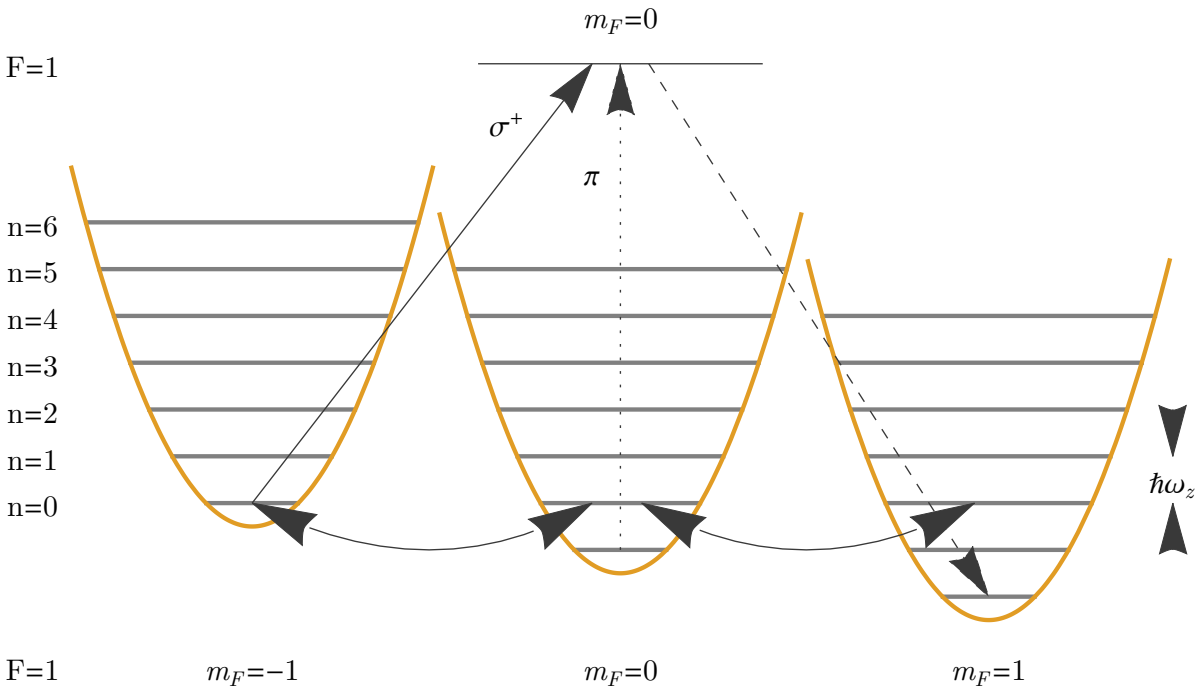

Fig. 6: Simple scheme for degenerate Raman sideband cooling. The lattice light induced degenerate two-photon transitions between adjacent magnetic hyperfine- and harmonic oscillator-levels (double arrows). Atoms are pumped (solid, dotted, dashed arrows) to $m_F = 1$ from where two-photon transitions take place reducing the motional quantum number. The m_F,n and $m_F - 1$,$n - 1$-states are shifted to degeneracy by the Zeeman effect.

Neglecting the light-shift introduced by the Raman-pump beam for the $|F = 1,m_F = -1\rangle$ and $|F = 1,m_F = 0\rangle$ levels, we consider an atom initially prepared in $|F = 1,m_F = 1\rangle$.

The atoms were loaded into the lattice after the MOT-phase and optical pumping into the the $F = 1$ hyperfine state. The sample is initially not spin polarized but nevertheless considering the evolution of an individual atom in $|F = 1,m_F = 1\rangle$ also covers the evolution of an atom in the other two states. The atom's motional quantum state in the lattice is denoted by n. We will write the complete state as e.g. $|F = 1,m_F = 1,n = 5\rangle$ omitting the $F =$, etc. in the further discussion. A magnetic field shifts the adjacent states $|1,m_F,n\rangle$ and $|1,m_F + 1,n - 1\rangle$ into degeneracy allowing degenerate two-photon Raman transitions between these two states. The two-photon coupling is induced by the lattice light. So the atom initially in $|1,1,5\rangle$ now arrives in $|1,0,4\rangle$, where it can conduct a two-photon transition either back to $|1,1,5\rangle$ or further to $|1,-1,3\rangle$.

As the atom has lost two quanta of kinetic energy in $|1,-1,3\rangle$, it would be favorable to admit a further reduction of the kinetic energy, hence the atom is optically pumped by σ^+-light to the $F = 0$-state from where it decays either to $|1,0,3\rangle$ or to $|1,1,3\rangle$. The motional quantum number does not change on average since the atom is in the Lamb-Dicke regime. From that point on the atom conducts the same processes over and over until it finally reaches the dark-state $|1,1,0\rangle$. If the atom reached the motional ground state in $|1,0,0\rangle$, it would not be able to get to the dark-state, hence the optical pumping also has a small π-component, which pumps the atom to $F = 0$ from where it will decay to the dark-state at some point. $|1,1,0\rangle$ is called dark-state because the optical pumping with its polarization does not couple to this state (ignoring transitions to higher F-levels). In a perfect isotropic potential structure this situation would occur for all three directions but as this is not the

case in the situation discussed below further assumptions are made in subsection 4.2.

4. Calculation of the Lattice Potential

4.1. Derivation of the Light-Induced Potential for a 2-Level System

The potential arises from the interaction of an atom with an electric field. In the special case of an atom interacting with a fast oscillating electric field of light it can be explained considering a two-level atom coupled to a classical monochromatic light-field

$$\vec{E}(\vec{r},t) = \mathrm{Re}[\vec{E}_L(\vec{r})\exp(-i\omega_L t)]. \tag{14}$$

The resulting Hamiltonian for the atom with ground state $|g\rangle$ and excited state $|e\rangle$ reads

$$\hat{H}_A = \hbar\omega_e |e\rangle\langle e|, \tag{15}$$

where the ground state's energy is zero and the excited state's energy is $E_e = \hbar\omega_e$. The coupling between the two states is created by the interaction of the atom and the field. The Hamiltonian is given by

$$\hat{H}_I = -\hat{\vec{d}}\cdot\vec{E}_L(t) = \frac{\hbar\Omega}{2}\exp(i\omega_L t)|g\rangle\langle e| + \frac{\hbar\Omega^*}{2}\exp(-i\omega_L t)|e\rangle\langle g| \tag{16}$$

in the dipole-approximation, where the light's wavelength is long compared to the extent of a single atom, so that the field does not vary on the scale of an atom. Here $\hat{\vec{d}} = -e\vec{r}$ denotes the transition dipole moment. The last term assumes the rotating-wave-approximation. This approximation is valid if the detuning $\Delta = \omega_L - \omega_e \ll \omega_e$ is relatively small compared to the resonant transition, this is linked to the fact that the assumption of a two level system is valid. The coupling strength $\Omega = \langle g|e\vec{r}\cdot\vec{E}_L|e\rangle/\hbar$, called Rabi frequency, also has to be small compared to the optical frequency $|\Omega| \ll \omega_e$, so that the rotating-wave-approximation is still valid. Writing the atomic state as $\Psi(t) = c_g|g\rangle + c_e|g\rangle$, plugging it into the Schrödinger equation

$$i\hbar\partial_t\Psi(t) = (\hat{H}_A + \hat{H}_I)\Psi(t) \tag{17}$$

and using the substitution $\tilde{c}_e = c_e\exp(i\omega_L t)$, one can obtain the resulting Hamiltonian

$$\hat{H} = -\hbar(\omega_L - \omega_e)|e\rangle\langle e| + \frac{\hbar\Omega}{2}|g\rangle\langle e| + \frac{\hbar\Omega^*}{2}|e\rangle\langle g|. \tag{18}$$

This result can be written in matrix form, we obtain

$$\hat{H} = \begin{pmatrix} 0 & \frac{\hbar\Omega}{2} \\ \frac{\hbar\Omega^*}{2} & -\hbar\Delta \end{pmatrix}, \tag{19}$$

where $\Delta = \omega_L - \omega_e$ is the detuning from resonance. The resulting dynamics can be calculated with a density matrix

$$\rho = \sum_{m,n}|m\rangle\rho_{m,n}\langle n|, \tag{20}$$

where $\langle m|$ and $\langle n|$ denote an orthonormal basis, here it reads

$$\rho = \begin{pmatrix} \rho_{gg} & \rho_{ge} \\ \rho_{eg} & \rho_{ee} \end{pmatrix} = \begin{pmatrix} |c_g|^2 & c_g\tilde{c}_e^* \\ \tilde{c}_e c_g^* & |\tilde{c}_e|^2 \end{pmatrix}. \tag{21}$$

Since an atom can also decay spontaneously from the excited state, additional terms are added to the Hamiltonian, these can be derived via Weisskopf-Wigner theory of spontaneous emission [Scully and Zubairy, 1997]. The additional Lindblad operator

$$\hat{L} = \begin{pmatrix} \Gamma\rho_{ee} & -\frac{\Gamma}{2}\rho_{ge} \\ -\frac{\Gamma}{2}\rho_{eg} & -\Gamma\rho_{ee} \end{pmatrix}, \tag{22}$$

describes the spontaneous decay between the excited and ground state, where $\Gamma = \frac{\omega_e^3 |\langle \hat{\vec{d}} \rangle|^2}{3\pi\epsilon_0 \hbar c^3}$ denotes the natural line width. We assume that the rates at which the atom's state changes act independent and can simply be added [Cohen-Tannoudji *et al.*, 2004]. The von Neumann equation

$$\partial_t \rho = -\frac{i}{\hbar}[\hat{H},\rho] + \hat{L} \tag{23}$$

now yields four coupled differential equations, of which only 2 are independent as it holds that $\rho_{ee} + \rho_{gg} = 1$ and $\rho_{ge} = \rho_{eg}*$. Therefore one has to find a solution to two coupled differential equations.

$$\partial_t \rho_{gg} = \Gamma\rho_{ee} + \frac{i}{2}(\Omega^*\rho_{ge} - \Omega\rho_{eg}) \tag{24}$$

$$\partial_t \rho_{ee} = -\Gamma\rho_{ee} + \frac{i}{2}(\Omega\rho_{eg} - \Omega^*\rho_{ge}) \tag{25}$$

$$\partial_t \rho_{ge} = -\left(\frac{\Gamma}{2} + i\Delta\right)\rho_{ge} + \frac{i}{2}\Omega(\rho_{gg} - \rho_{ee}) \tag{26}$$

$$\partial_t \rho_{eg} = -\left(\frac{\Gamma}{2} - i\Delta\right)\rho_{eg} + \frac{i}{2}\Omega^*(\rho_{ee} - \rho_{gg}) \tag{27}$$

A steady state solution makes sense if the atom's internal evolution is faster than the timescale in which it travels over the distance of the light's wavelength but not for timescales in which it changes its internal state, ergo $\omega_L \ll t^{-1} \ll \max[\Gamma,\Omega]$. The steady state solution can be obtained setting the time derivatives $\partial_t \rho_i = 0$,

$$\rho_{ee} = \frac{|\Omega|^2}{\Gamma^2 + 4\Delta^2 + 2|\Omega|^2} \tag{28}$$

$$\rho_{ge} = \frac{(i\Gamma + 2\Delta)\Omega}{\Gamma^2 + 4\Delta^2 + 2|\Omega|^2}. \tag{29}$$

To derive a (conservative) force and from that on a potential, we consider a semi-classical force. Noting that $\partial_t \vec{p} = \vec{F}$, we can find the average force expectation value $\partial_t \langle \hat{p} \rangle$ with the help of the Ehrenfest theorem

$$\begin{aligned} \partial_t \langle \hat{p} \rangle &= \frac{1}{i\hbar} \langle [\hat{p},\hat{H}] \rangle \\ &= -\langle [\vec{\nabla},\hat{H}] \rangle \\ &= -\operatorname{Tr}[\tilde{\rho}[\vec{\nabla},\hat{H}]]. \end{aligned} \tag{30}$$

The Hamiltonian in this case does not only respect the atom's internal degrees of freedom but also the external ones, therefore the Hamiltonian $\hat{H}_{\text{res}}$ consists of the spontaneous decay Hamiltonian $\hat{H}_{\text{spont}}$ as well as the atom-light interaction Hamiltonian $\hat{H}_{\text{int}}$ and the kinetic energy term of the atom

$$\hat{H}_{res} = \frac{\hat{p}^2}{2m} + \hat{H}_{\text{spont}} + \hat{H}_{\text{int}}. \tag{31}$$

We note that the momentum and position operators are now acting on the atom's momentum and position, therefore the electric field can depend on the position, therefore also the coupling strength. We now plug Equ. 31 into Equ. 30, it yields

$$\begin{aligned}\langle\vec{F}\rangle &= -\operatorname{Tr}[\tilde{\rho}[\vec{\nabla},\hat{H}_{\text{int}}]] \\ &= -\vec{\nabla}\left(\frac{\hbar\Omega}{2}\right) \\ &= -\frac{\hbar}{2}\left[(\vec{\nabla}\Omega(\vec{r}))\rho_{eg} + (\vec{\nabla}\Omega^*(\vec{r}))\rho_{ge}\right]\end{aligned}$$

with $\Omega(\vec{r}) = |\Omega(\vec{r})|\exp(i\phi(\vec{r}))$

$$= -\hbar\left\{(\vec{\nabla}|\Omega(\vec{r})|)\operatorname{Re}[\exp(i\phi(\vec{r}))\rho_{eg}] - |\Omega(\vec{r})|(\vec{\nabla}\phi(\vec{r}))\operatorname{Im}[\exp(i\phi(\vec{r}))\rho_{eg}]\right\}$$

Using the steady-state solutions from Equ. 29 we obtain for the semi-classical force

$$\langle\vec{F}\rangle = -\hbar\left(\frac{\Delta\vec{\nabla}|\Omega(\vec{r})|^2}{\Gamma^2+4\Delta^2+2|\Omega|^2} + \frac{|\Omega(\vec{r})|^2\Gamma\vec{\nabla}\phi(\vec{r})}{\Gamma^2+4\Delta^2+2|\Omega|^2}\right), \tag{32}$$

we note that the time dependence is still there but its hidden in ρ_{ge}. The first term corresponds to a reactive force, the second term to dissipative force since it varies with the phase of the Rabi frequency, which depends on the electric field's phase. Another approach to derive this result would be to consider the driven atom as having an induced dipole moment $\langle\hat{\vec{d}}\rangle$, the resulting Potential would then be $U(\vec{r},t) = \langle\hat{\vec{d}}\rangle\,\vec{E}(\vec{r},t)$. In the far-off-resonant limit $\Omega,\Gamma \ll \Delta$ one can rewrite the force as

$$\langle\vec{F}\rangle = -\hbar\left(\frac{\vec{\nabla}|\Omega(\vec{r})|^2}{4\Delta} + \frac{|\Omega(\vec{r})|^2\Gamma\vec{\nabla}\phi(\vec{r})}{4\Delta^2}\right). \tag{33}$$

We can then find a (time averaged) potential using $F = -\vec{\nabla}U(\vec{r})$, rewriting $|\Omega|^2$ in terms of the line width Γ and the intensity $I(\vec{r}) = \frac{\epsilon_0 c\overline{|\vec{E}(\vec{r})|^2}}{2}$, the bar denotes time averaged value, the first term reads

$$U_{dip}(\vec{r}) = \frac{3\pi c^2\Gamma}{2\omega_e^3\Delta}I(\vec{r}), \tag{34}$$

where c denotes the speed of light. We see that the potential has a minimum at the maximum intensity for negative detuning and vice versa.

4.2. Resulting Lattice and Approximation

4.2.1. The Polarizability Tensor

In a real system the 2-level approximation does often not describe the full physics. An easy approach is to introduce the coupling of a (optically pumped) hyperfine ground state F to multiple hyperfine excited states F' via an light-shift operator [Deutsch and Jessen, 1998]

$$\hat{U}(\vec{r}) = \vec{E}_L(\vec{r})^* \sum_{\substack{F',m\\m',m''}} \frac{|F,m\rangle\langle F,m|\,\hat{\vec{d}}\,|F',m'\rangle\langle F',m'|\,\hat{\vec{d}}\,|F,m''\rangle\langle F,m''|}{\hbar\Delta_{F\to F'}}\vec{E}_L(\vec{r}), \tag{35}$$

here $\Delta_{F\to F'}$ denotes the detuning from the $F \to F'$-transition. It is composed of the electric field and a polarizability tensor. This tensor contains the coupling terms between different states coupled by two photons. We can rewrite this expression in terms of reduced matrix elements, Wigner 3-j and

Wigner 6-j symbols separately for each polarization component σ. The common transition symbols σ^+, π and σ^- correspond to $\sigma = -1$, $\sigma = 0$ and $\sigma = 1$. The Wigner 3-j symbols yield zero unless it holds that $m_F = m'_F + q$.

$$\langle F,m|\hat{d}_\sigma|F',m'\rangle = (-1)^{F-m}\sqrt{2F+1}\begin{pmatrix} F & 1 & F' \\ -m & \sigma & m' \end{pmatrix}\langle F\|\hat{\vec{d}}\|F'\rangle \tag{36}$$

$$\begin{aligned} &= (-1)^{F-m+F'+J+1+I}\sqrt{(2F+1)(2F'+1)(2J+1)} \\ &\times \begin{pmatrix} F & 1 & F' \\ -m & \sigma & m' \end{pmatrix}\begin{Bmatrix} J & J' & 1 \\ F' & F & I \end{Bmatrix}\langle J\|\hat{\vec{d}}\|J'\rangle \end{aligned} \tag{37}$$

$$\begin{aligned} \langle F',m'|\hat{d}_{-\sigma'}|F,m''\rangle &= (-1)^{F'-m'+F+J'+1+I+\sigma'}\sqrt{(2F+1)(2F'+1)(2J+1)} \\ &\times \begin{pmatrix} F' & 1 & F \\ -m' & -\sigma' & m'' \end{pmatrix}\begin{Bmatrix} J' & J & 1 \\ F & F' & I \end{Bmatrix}\langle J'\|\hat{\vec{d}}\|J\rangle\,. \end{aligned} \tag{38}$$

For a component σ of a tensor operator of rank k it holds that $(T^{(k)}_\sigma)^\dagger = (-1)^\sigma T^{(k)}_{-\sigma}$ having that in mind one can derive a link between the two reduced matrix elements from above [Steck, 2007], it follows

$$\langle J'\|T^{(k)}\|J\rangle = (-1)^{J'-J}\sqrt{\frac{2J+1}{2J'+1}}\langle J\|T^{(k)}\|J'\rangle^*\,. \tag{39}$$

Together with symmetries of the Wigner 6-j symbols [Edmonds, 1957] [Edmonds, 1957] [Edmonds, 1957]we can write the whole expression in a more compact form

$$\begin{aligned} &\langle F,m|\hat{d}_\sigma|F',m'\rangle\langle F',m'|\hat{d}_{-\sigma'}|F,m''\rangle = \\ &(-1)^{2I+2J'-m-m'+\sigma'}(2F+1)(2F'+1)(2J+1) \\ &\times \begin{pmatrix} F & 1 & F' \\ -m & \sigma & m' \end{pmatrix}\begin{pmatrix} F' & 1 & F \\ -m' & -\sigma' & m'' \end{pmatrix}\begin{Bmatrix} J & J' & 1 \\ F' & F & I \end{Bmatrix}^2\left|\langle J\|\hat{\vec{d}}\|J'\rangle\right|^2 \end{aligned} \tag{40}$$

Note that the inversion of the second polarization term σ' implicates that the polarization is now always in the same frame, e.g. a Raman transition $m_F \to m_F + 1 \to m_F$ corresponds to σ^+ light in both cases. Evaluating the sum in Equ. 35 for each polarization combination yields nine matrices (cf. Appendix B). We assume that the introduced Zeeman splitting and the splitting between the excited hyperfine states is much smaller than the laser detuning from resonance

$$\Delta_{Zeman} \ll \Delta_{HFS'} \ll \Delta. \tag{41}$$

The detuning in Equ. 35 then simplifies to one fixed value Δ. The sum can be evaluated on a sub space as big as possible also taking $n = 6$, etc. states into account, but as we are interested in the coupling between the $|F = 1,m_F\rangle$ levels we sum over all excited states of the $5^2P_{3/2}$ state and take m_F and m''_F of the $F = 1$ ground state. This assumption is valid, if the detuning from other excited states is huge compared to the detuning from resonance of one specific transition. The detuning from the D_1-line for example is in the order of THz while the detuning from the D_2 line is on the order of GHz.

An alternative representation of the light shift operator Equ. 35 in the limit of a detuning greater then the excited state hyperfine splitting reads

$$\hat{U}_F(\vec{r}) = \frac{\left|\langle J\|\hat{\vec{d}}\|J'\rangle\right|^2}{12\hbar\Delta_{F_{max}\to F'_{max}}}\left(2\left|\vec{E}_L(\vec{r})\right|^2\hat{1} + i[\vec{E}_L(\vec{r})^* \times \vec{E}_L(\vec{r})]\frac{\hat{\vec{F}}}{F}\right). \tag{42}$$

The double bars indicate the reduced matrix element [Steck, 2001], the states F_{max} describe the stretched states $F_{max} = I + J$ where I and J are the quantum numbers for nuclear spin and total angular momentum. $\hat{1}$ represents the identity operator, and $\frac{\hat{\vec{F}}}{F}$ is the (dimensionless) total spin operator. We can see that there are off-diagonal terms in the potential (cf. Appendix B). These terms introduce the coupling between different magnetic hyperfine states, the potential therefore depends on the magnetic state of the atom. The first term of $\hat{U}_{F_{max}}(\vec{r})$ can be rewritten to obtain Equ. 34 again.

Evaluating Equ. 35 for each polarization combination separately, we obtain nine three dimensional square matrices for the subspace of the lower hyperfine ground state $F = 1$. With two-photon transitions coherences between levels with $\Delta m_F = 0, \pm 1, \pm 2$ occur, but in the limit of infinite detuning the coherences for $\Delta m_F = \pm 2$ vanish. The resulting matrices are depicted in Appendix B. Calculating the transition frequencies and potentials can be done in the usual Cartesian coordinate system or in the spherical basis. The spherical basis vectors are made up of the Cartesian basis vectors as follows

$$\begin{aligned} \vec{e}_{+1} &= -\frac{1}{\sqrt{2}}(\vec{e}_x + i\vec{e}_y) \\ \vec{e}_{-1} &= \frac{1}{\sqrt{2}}(\vec{e}_x - i\vec{e}_y) \qquad (43) \\ \vec{e}_0 &= \vec{e}_z, \end{aligned}$$

$$\text{it holds that} \qquad \vec{e}_q{}^* = (-1)^q \vec{e}_{-q}. \qquad (44)$$

A vector field $\vec{F} = F_x\vec{e}_x + F_y\vec{e}_y + F_z\vec{e}_z$ can be transformed to the spherical basis by a linear transformation

$$\begin{pmatrix} F_{+1} \\ F_{-1} \\ F_0 \end{pmatrix} = \frac{1}{\sqrt{2}} \begin{pmatrix} -1 & i & 0 \\ 1 & -i & 0 \\ 0 & 0 & \sqrt{2} \end{pmatrix} \cdot \begin{pmatrix} F_x \\ F_y \\ F_z \end{pmatrix}. \qquad (45)$$

Applying this transformation to the electric field we obtain the electric field components for each polarization. We see that the two circular polarized beams always have the same intensity at each point in space, therefore the diagonal part of the resulting potential is the same for all m_F states. The quantization axis points along the magnetic field in positive z-direction. The resulting potential is calculated in the following.

4.2.2. Calculation of the Lattice Characteristics

The potential can be designed such that the potential shows a periodic structure in each direction. A simple setup could consist of four interfering beams to create a three dimensional lattice-like structure. This resulting potential landscape is called optical lattice. The lattice described in subsubsection 2.3.2 can not be described as aesthetic as an optical lattice derived from orthogonal beams could be described. Nevertheless we can calculated the characteristics of that potential numerically. In principle there happen a lot of fascinating phenomena if an atom is stored in an optical lattice, e.g. an atom can tunnel through the potential barrier or it can be excited to a state which is not trapped and simply fly away and be trapped again after a relaxation process. But as we are interested in cooling a sample of atoms we will consider a regime, where we can neglect the coupling of the internal state and the external (movement) state. In order to motivate this approximation we will first consider the potential produced by four interfering beams. Each beam is collimated to a $1/e^2$ beam waist $w_0 = 1.1\,\text{mm}$ and carries $P_j = 50\,\text{mW}$ of power, the laser is $\Delta = -6.835\,\text{GHz}$ detuned from resonance of the D_2-line. To gain some intuition for the overall structure, the potential's energy-isosurfaces are depicted in Fig. 7.

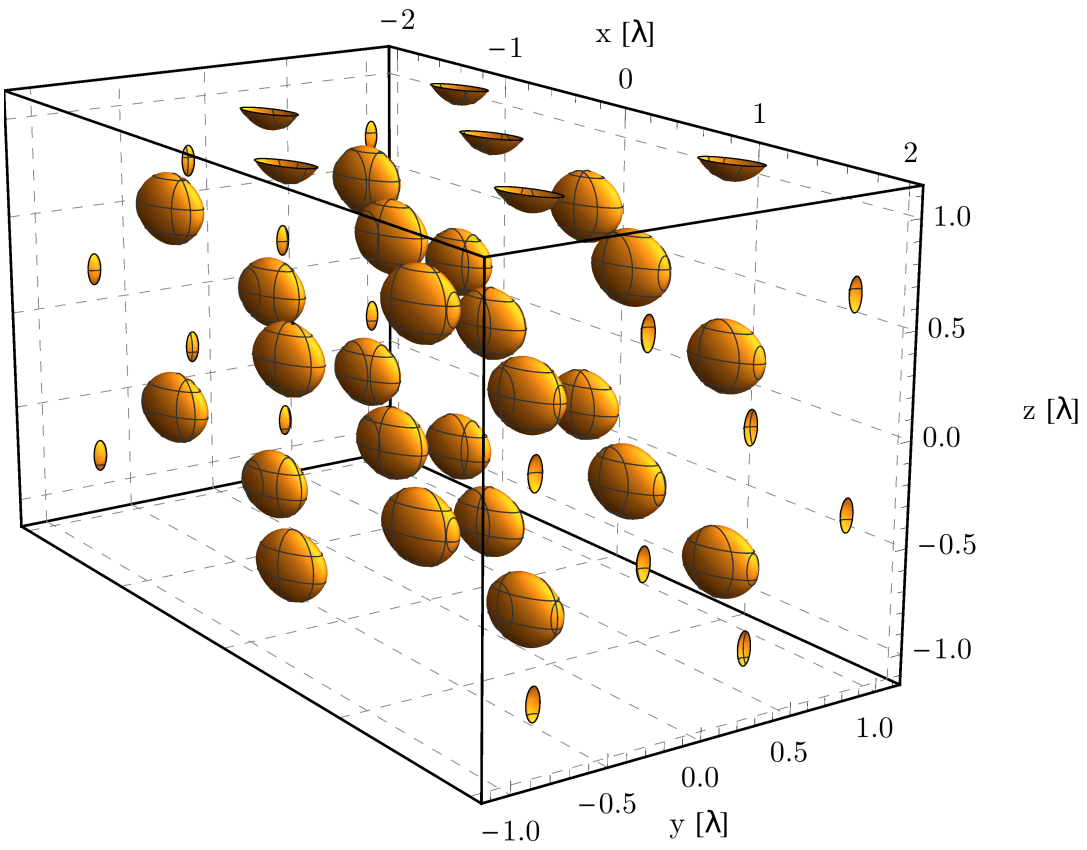

Fig. 7: The resulting iso-energy-surfaces solving $U_{dip}(\vec{r}) = -1800\, E_{recoil}$ in the given configuration. The principal axes of the depicted ellipsoid do not coincide with the lights' propagation axes, therefore the lattice has to be approximated along the principal axis near the potential minima.

The four beams' wave vectors and electric fields read as follows,

$$\vec{k}_{\text{refl, in}} = k_0 \cdot (\sin(\alpha), -\cos(\alpha), 0)^\tau \tag{46}$$

$$\vec{k}_{\text{trans, horz}} = k_0 \cdot (-\sin(\alpha), -\cos(\alpha), 0)^\tau \tag{47}$$

$$\vec{k}_{\text{trans, vert}} = k_0 \cdot (0,0,1)^\tau \tag{48}$$

$$\vec{E}_{\text{refl, in}} = E_0 \cdot \frac{1}{\sqrt{2}}(\cos(\alpha), Sin(\alpha), 1)^\tau \tag{49}$$

$$\vec{E}_{\text{trans, horz}} = E_0 \cdot (0,0,1)^\tau \tag{50}$$

$$\vec{E}_{\text{trans, vert}} = E_0 \cdot (-\sin(\alpha), -\cos(\alpha), 0)^\tau, \tag{51}$$

$k_0 = \frac{2\pi}{\lambda}$ is the wave vector's absolute value, E_0 denotes the maximum electric field amplitude. The angle α is the absolute value between each beam and the y-axis. The resulting electric field distribution is then calculated as a sum over all four beams, the reflected beam has the same polarization and the opposite wave vector $-\vec{k}_{\text{refl, in}}$ compared to the incoming beam. The resulting field made of 4 Gaussian beams reads

$$\vec{E}_L(\vec{r}) = \sum_j \frac{\vec{E}_j}{1 - i\frac{|\hat{r}\cdot\vec{k}_j/k_0| - d_j}{z_R}} \exp\left[\frac{\left|\hat{r}\cdot\left(\frac{\vec{E}_j}{E_0}\times\frac{\vec{k}_j}{k_0}\right)\right|^2 + \left|\hat{r}\cdot\frac{\vec{E}_j}{E_0}\right|^2}{w_0^2\left(1 - i\frac{|\hat{r}\cdot\vec{k}_j/k_0| - d_j}{z_R}\right)}\right] \exp[i(\vec{k}_j\cdot\vec{r} - d_j k_0)], \tag{52}$$

where $\hat{r}$ is a matrix with x,y,z on the diagonal, d_j is the distance from the beams focus, $z_R = \frac{\pi w_0^2}{\lambda}$ is the Rayleigh range and w_0 the beam waist [Boyd, 2008]. The index j represents the four beams' indices. The distance from the focus is assumed to be the same for all three running waves $d_{running} = 20\,\text{cm}$ and the retroreflected beam travels twice that distance after the fiber collimator ergo $d_{reflected} = 40\,\text{cm}$.

The potential then consists of a local lattice like part and a part creating a spacial confinement in the focus of the beam. The first part has a periodic structure where the potential minima are approximately distanced by λ along the running beams and by $\lambda/2$ along the reflected beam. This result is exact for a lattice made of perpendicular beams. The resulting lattice can be plotted in different plains, the result is depicted in Fig. 8.

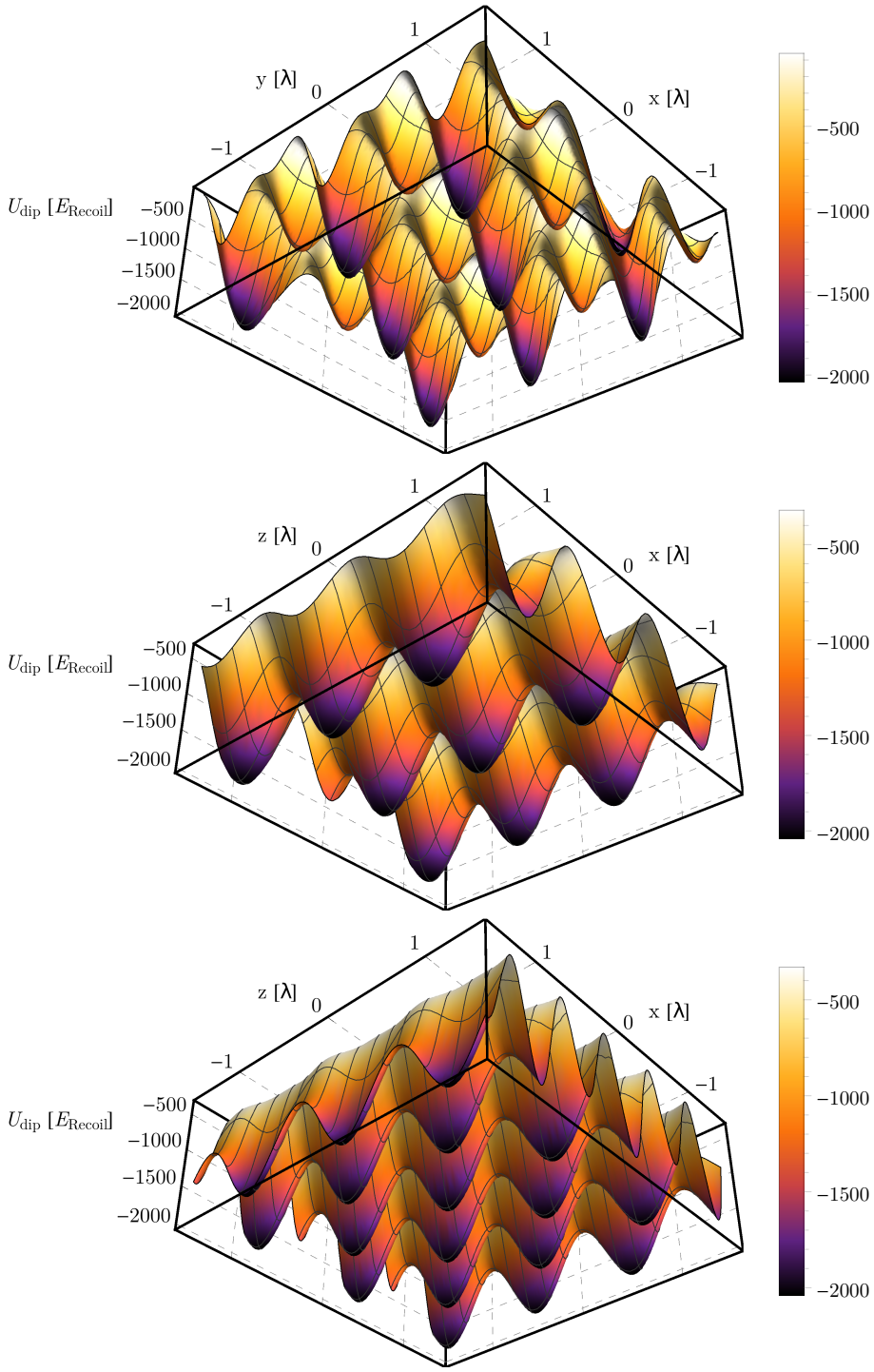

Fig. 8: The lattice potential in different plains. The remaining sample point is chosen such that the potential has a local minimum there. (**Top**) The potential in the x-y-plain, the z-sample point corresponds to $z_S \approx 0.2\,\lambda$ in Fig. 7. (**Middle**) x-z-plain, $y_S \approx 0.4\,\lambda$. (**Bottom**) y-z-plain, $x_S \approx 0.0\,\lambda$.

Looking at the potentials in Fig. 8, we see that the shape should correspond to an three dimensional harmonic oscillator around the minima. Therefore we fit a hypersurface around the potential minimum and transform the coefficient array to diagonal form (according to the principal-axis-theorem) to eventually obtain the spring constant and therefore the oscillation frequency. We will consider later, why it makes sense to approximate the potential as an harmonic oscillator. The resulting

oscillation frequencies are depicted in Fig. 9, the lattice along the coordinate axis is also shown. The maximum oscillation frequencies as well as the lattice depth also stated in Tab. 1.

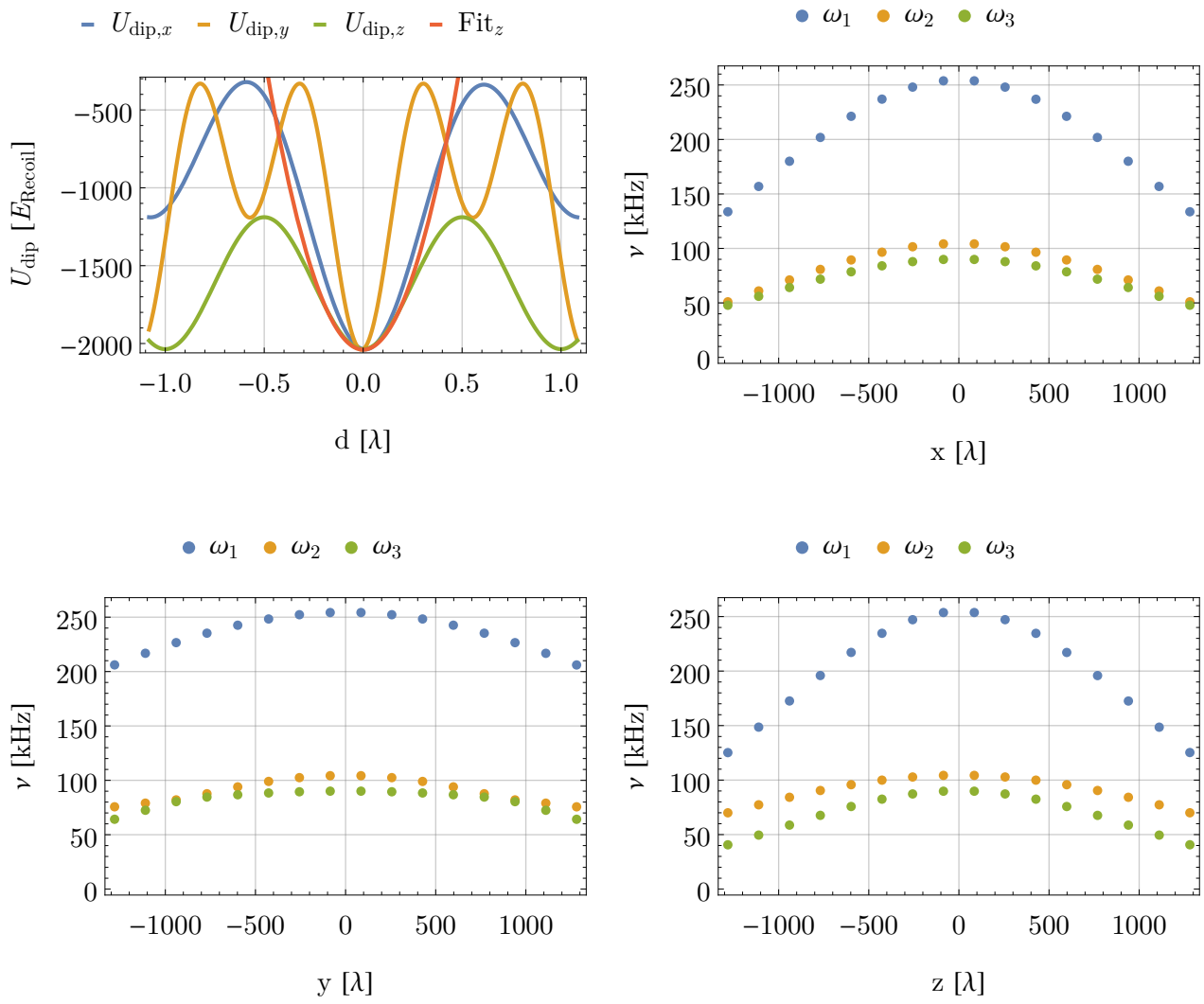

Fig. 9: Potential and harmonic approximation and spacial behavior of the oscillation frequencies. (**Top Left**) Lattice potentials along the coordinate axis. The depicted approximation is also correct in this frame due to the point symmetry in the x-y-plain with respect to the origin, this symmetry only holds for plain waves exactly but is also mostly valid in the center of a Gaussian beam. Therefore one principal axis is always pointing in z-direction. There are less bound vibrational states along the less confining z-axis than in the other directions. (**Top Right**) The Oscillation frequency decreases along the x-axis if the distance from the perfect intersection of the beams gets bigger due to their Gaussian beam shape, the result is similar to the variation along z. (**Bottom Left**) The oscillation frequency along the y-axis decreases slower than in x- or z-direction. (**Bottom Right**) Oscillation frequency along the z-axis.

Tab. 1: Resulting oscillation frequencies and lattice depths along the principal axis r_i around a central minimum. Calculated for parameters $w_0 = 1.1\,\mathrm{mm}$ $P_j = 50\,\mathrm{mW}$ and $\Delta = -6.835\,\mathrm{GHz}$

Quantity	r_1	r_2	r_3
Lattice depth $[E_{recoil}]$	1976	1879	1195
Lattice depth $[\mu\mathrm{K}]$	357.6	340.1	216.4
Oscillation frequency ω $[2\pi\cdot\mathrm{kHz}]$	254.5	104.5	90.1
Level spacing $\hbar\omega$ $[\mu\mathrm{K}]$	12.2	5.0	4.3

4.2.3. Motivating the Harmonic Oscillator Approximation

As an atom is not a classical particle, it's external, mechanical state has to be calculated quantum mechanically. In a periodic potential the wave function shows the same periodicity as the potential (Bloch's theorem [Bloch, 1929]), if a particle is localized a description in terms of delocalized Bloch waves makes less sense since we have a well localized wave function around each lattice site. The resulting wave function can be described in terms of Wannier functions, which also account for tunneling between neighboring lattice sites. To motivate the harmonic approximation consider a one dimensional periodic potential, e.g. an atom in the light field of a standing wave,

$$U(x) = U_0 \sin^2\left(\pi \frac{x}{\lambda/2}\right) \tag{53}$$

If the atoms kinetic energy is sufficiently small, it will be localized around a potential minimum, thus we can expand the potential in the dimensionless parameter $\frac{x}{\lambda/2}$ which yields

$$U(x) \approx U_0 \left(\pi \frac{x}{\lambda/2}\right)^2. \tag{54}$$

The same approach is still valid for a multidimensional periodic structure. In a three dimensional harmonic oscillator potential the Hamiltonian

$$\hat{H}_{mech} = \frac{\hat{\vec{p}}^2}{2m} + \frac{m}{2}\sum_{q=1}^{3} \omega_i r_i^2 \tag{55}$$

describes the atom, where $\hat{\vec{p}} = -i\hbar\vec{\nabla}$ is the momentum operator, m the mass of an atom and the index q describes three (orthogonal) dimensions with oscillation frequency ω_q. The Hamiltonian can be separated in each direction therefore the resulting states are product states. The solution are the well known number states $|n_1\rangle\,|n_2\rangle\,|n_3\rangle$, the Hamiltonian can be rewritten as

$$\hat{H}_{mech} = \sum_{q=1}^{3} \hbar\omega_q (a_q^\dagger a_q + \frac{1}{2}). \tag{56}$$

Here we introduced the creation and annihilation operators $a_q^\dagger$ and a_q, the link between these two notations is given by

$$a_q = \sqrt{\frac{m\omega_q}{2\hbar}}\left(r_q + \frac{i}{m\omega_q}\hat{p}_q\right). \tag{57}$$

The creation operator creates one energy quantum of $\hbar\omega_q$ in direction q, the adjoint annihilation operator removes one quantum.

4.2.4. Raman Coupling

We saw in subsection 3.1 that adjacent vibrational levels are coupled by light. All beams have the same (absolute value) wave vector. The momentum transfer after the two photon process to the atom depends on the angle under which the photons interact with the atom. If the absorbed and emitted photon propagate in the same direction no momentum will be transferred, while the atom gains $2\hbar k$ of momentum if the emitted photon propagates in the opposite direction of the absorbed photon. We will therefore assume an average value of k, furthermore that each principal axis of a three dimensional potential minimum in the lattice couples to one beam. This beam would then stimulate two photon processes transferring momentum to the atoms. In principle one should consider the radiation pattern of the atom and derive an expression for the average wave vector difference but due to the fact that we also have uncertainties in the magnetic field changing the polarization of the electric fields the assumption of $\hbar k$ will be sufficient.

We assumed that the atoms are well localized around each potential minimum, to estimate the magnitude of the coherent transitions between two levels we will calculate the electric field strengths at a lattice minimum and sum over all couplings induced by each polarization combination. For example an atom in $m_F = 1$ having (n_1,n_2,n_3) motional quanta will be coupled to $m_F = 0$ by combinations of π, σ^+ and σ^-,π.

The electric field components in a central minimum of the lattice ($P_j = 50\,\mathrm{mW}$, e^{-2}-radius = $1.1\,\mathrm{mm}$, $\Delta = 6.835\,\mathrm{GHz}$) are

$$E_{+1} = (-3763 + 3378i)\,\mathrm{V/m} \tag{58}$$
$$E_{-1} = (3763 + 3378i)\,\mathrm{V/m} \tag{59}$$
$$E_0 = 7489\,\mathrm{V/m}. \tag{60}$$

To calculate the coupling we take the results from Appendix B, as already stated we'll consider the coupling between $m_F = 1$ and $m_F = 0$.

$$\begin{aligned} U_{coupling} =& \frac{\left|\langle J\|\hat{\vec{d}}\|J'\rangle\right|^2}{\hbar\Delta}\big(E_0^* \langle F=1,m_F=1|M_{\pi,\sigma^+}|F=1,m_F=0\rangle E_{-1} \\ &+ E_{+1}^* \langle F=1,m_F=1|M_{\sigma^-,\pi}|F=1,m_F=0\rangle E_0\big) \\ =& \underbrace{(134+120i)\,E_{recoil}}_{\text{from the first term}} + \underbrace{(134-120i)\,E_{recoil}}_{\text{from the second term}} = 268\,E_{recoil} \end{aligned} \tag{61}$$

As already shown in subsection 3.1 the atom does also change its motional quantum number in some cases. The transition probability scales with the Lamb-Dicke parameter η_q and the number of quanta in each direction n_q, with the oscillation frequencies from Tab. 1 we find

$$\begin{aligned} \eta_1 &= 0.12 \\ \eta_2 &= 0.19 \\ \eta_3 &= 0.20 \end{aligned} \tag{62}$$

The sum over all three directions yields the coupling strength for transitions lowering the motional quantum number

$$U_{coupling} \cdot (\sqrt{n_1}\eta_1 + \sqrt{n_2}\eta_2 + \sqrt{n_3}\eta_3) = (\sqrt{n_1}\cdot 33 + \sqrt{n_2}\cdot 51 + \sqrt{n_3}\cdot 55)\,E_{recoil} \tag{63}$$
$$= (\sqrt{n_1}\cdot 123 + \sqrt{n_2}\cdot 192 + \sqrt{n_3}\cdot 207)\,\mathrm{h}\cdot\mathrm{kHz}, \tag{64}$$

h denotes Planck's constant. The couplings $m_F = 1 \to m_F' = 0$ and $m_F = 0 \to m_F' = 1$ are equal since we did not take the individual detuning between the single magnetic hyperfine states into account. That fact in mind we consider the case of $m_F = -1 \to m_F' = 0$. The two states get coupled by π,σ^- light as well as σ^+,π because this light couples to the same states like in the previous case just with opposite sign.

4.2.5. Linewidth of the Raman transitions

The linewidth of the Raman transition is important since it determines whether a transition between adjacent magnetic resolves the level structure of the motional states. The spontaneous transition rate induced by the polarization component σ is [Cline *et al.*, 1994]

$$\gamma_{\sigma,F,m_F\to F',m'_F} = \frac{6\pi c^3(\omega_0+\Delta)^3\epsilon_0|E_\sigma|^2}{h\left|\langle J\|\hat{\vec{d}}\|J'\rangle\right|^4}\left|\frac{\Gamma}{\omega_0^3\Delta}\sum_{\sigma',F'',m''_F}\langle F',m'_F|\hat{d}_{\sigma'}|F'',m''_F\rangle\,\langle F'',m''_F|\hat{d}_\sigma|F,m_F\rangle\right|^2. \tag{65}$$

The sum term can again be calculated in terms of reduced matrix elements, with the use of the matrices calculated before we can rewrite the expression

$$\gamma_\sigma = \frac{|E_\sigma|^2\left|\langle J\|\hat{\vec{d}}\|J'\rangle\right|^4(\omega_0+\Delta)^3}{\hbar^3\Delta^2 12\pi^2\epsilon_0 c^3}\left(\sum_{\sigma'}M_{\sigma',\sigma}\right)\circ\left(\sum_{\sigma'}M^*_{\sigma',\sigma}\right), \tag{66}$$

$A\circ B$ denotes the Hadamard or element-wise product of two matrices A and B of same dimensions. The total transitions are obtained by summing over all polarization components. The term can be understood as absorbing a photon from the laser field of polarization σ and then emitting a second photon spontaneously. The spontaneous scattering matrix reads

$$\gamma = \begin{pmatrix}2392 & 149 & 0\\ 149 & 2392 & 149\\ 0 & 149 & 2392\end{pmatrix}\text{Hz}. \tag{67}$$

The atoms get scattered ≈ 150 times each second spontaneously, therefore the motional energy levels are well resolved by the spontaneous Raman process. The diagonal elements correspond to Rayleigh scattering.

4.3. Scattering Rate and Estimated Cooling Rate

Another effect occurs if an atom interacts with a classical light field - power broadening. The absorption line gets wider with larger intensity driving the transition. Equ. 28 describes the population of a two level atom depending on the detuning Δ, linewidth Γ and Rabi frequency Ω. The Rabi frequency only appears squared, its square value is proportional to the intensity. With greater intensity occurs more off resonant scattering. Scattering which is not necessary to pump atoms in order to provide further reduction of the motional quantum number introduces heating. The effect of heating is an essential value if it comes to the estimation of heating in contrast to the provided heating.

The lattice detuning exceeds the excited states' hyperfine splitting, so it couples to all levels of the excited states' hyperfine states. The σ^+ and σ^- components of the lattice light have equal intensities, therefore they pump atoms at the same rates (neglecting the small detuning resulting from the Zeeman shift). We account for that by multiplying each ground state population in the two-level approximation by a factor of 1/3. The ground state of $F=2$ is assumed to have no population. The picture then reduces to the two-level system made up of each $|F=1,m_F\rangle$ level coupled to the whole $5^2P_{3/2}$ manifold. The squared Rabi frequency for this transition is made of the sum of the three polarization components,

$$\Omega^2_{res} = \sum_{\sigma=\{-1,0,1\}}|E_\sigma|^2\sum_{F',m'_F}\left|\langle F=1,m_F|\hat{d}_\sigma|F',m'_F\rangle\right|^2 = (384.5\cdot 2\pi\,\text{MHz})^2 \tag{68}$$

The ground state population is close to unity, $\approx 0.1\%$ of the atoms are in the excited state, resulting in a scattering rate of $4.8 \cdot 2\pi\,\mathrm{kHz}$. Taking less restrictive assumption with the use of [Grimm *et al.*, 2000]

$$\Gamma_{scatter}(\vec{r}) = \frac{\Gamma}{\hbar\Delta} U_{Dip}(\vec{r}), \tag{69}$$

we obtain a scattering rate of $6.9 \cdot 2\pi\,\mathrm{kHz}$. From this on we can calculate the expectable heating due to off resonant scattering of lattice light. The heating rate depends on the one hand on the trap geometry, on the other hand on the scattering rate and therefore also on the detuning and intensity. We assume that the heating occurs isotropic, which is not necessarily true since the absorption due to the laser happens in specified directions, whereas spontaneous emission is isotropic. The heating rate is discussed more in detail in [Grimm *et al.*, 2000], it is given by

$$\dot{T}_{heat} = \frac{2}{3} \frac{T_{rec}\Gamma_{scatter}}{1+\kappa}, \tag{70}$$

where the recoil temperature is $T_{recoil} = \hbar^2 k^2/(m k_B)$ and κ is a geometric factor, e.g. for a three dimensional harmonic trap it is $\kappa = 1$. With the values given above we obtain $\dot{T}_{heating} = 827\,\mu\mathrm{K/s}$.

The levels do also shift due to the repumper, since it is resonant to $F = 1 \rightarrow F' = 0$ the only level affected by the (almost) pure σ^+ light is the $m_F = -1$ level. The energy eigenvalues of a light dressed state result from diagonalizing Equ. 19, they read

$$E_{dressed\pm} = \frac{\hbar}{2}(-\Delta \pm \sqrt{\Delta^2 + |\Omega|^2}). \tag{71}$$

If the laser is on resonance the level gets shifted by $\hbar|\Omega|/2$. For the Raman-pump beam with 1 mW power and an beam waist of 1.1 mm we obtain $\Omega_{Raman-pump} = 13.9 \cdot 2\pi\,\mathrm{MHz}$, which shifts the levels by $\hbar\Omega_{Raman-pump}/2 = 6.95 \cdot h\,\mathrm{MHz}$.

To have a rough estimation of the scattering rate induced by the Raman-pump beam we assume that the transition is saturated and calculate the scattering rate similar to the two level approximation as $\Gamma_{Raman-pump} = 2\left(\frac{\Omega_{Raman-pump}}{\Gamma}\right)^2 \cdot \frac{\Gamma}{2} = 31.8 \cdot 2\pi\,\mathrm{MHz}$. This value is an absolute upper bound of the scattering rate for this transition since the atoms will get pumped to the other m_F states. The actual scattering rate does depend on the Raman transitions to the $m_F = -1$ level. For reference a power of $1\,\mu\mathrm{W}$ would result in an scattering rate of 31.9 kHz, which is closer to the values reported in [Fölling, 2003; Kerman *et al.*, 2000]. The transport rate from $m_F = -1$ to $m_F = 1$ is by a factor 1/3 smaller than the scattering rate since the relatxation from the $F = 0$,$m_F = 0$ level occurs with equal probability to each of the m_F ground states. Relaxation to $F = 2$ is neglected in this brief explanation.

The cooling efficiency should be determined by the two-photon Raman transitions since the Raman-pumping should be chosen to be much faster than the transitions lowering the motional quantum number. Each Raman transition removes - in the ideal case - one quantum of kinetic energy, assuming some mismatch and transitions between identical motional states we take half the transition rate between adjacent m_F levels. The geometric trap frequency is $\bar{\omega} = \sqrt[3]{\omega_1 \cdot \omega_2 \cdot \omega_3} = 133.8 \cdot 2\pi\,\mathrm{kHz}$, together with the geometric transition frequency of $\bar{\nu}_t rans = 170\,\mathrm{kHz}$ between adjacent m_F levels with the motional quantum numbers n and $n-1$ the cooling rate results in $\dot{T}_{cooling} = 0.54\,\mathrm{mK/s}$.

5. Conducted Measurements

An obvious sign of cooling nor heating was not observed to date - ipso facto the experimental steps and measurements conducted so far will be presented.

5.1. Magnetic Field Nullification

Stray magnetic fields disturb an atomic experiment due to the Zeeman effect. Therefore it is convenient to nullify stray magnetic fields as good as possible. In the presented work this was done utilizing microwave spectroscopy of atoms held in a far-off resonant dipole trap (ODT). The atoms were initially trapped in a magneto-optical trap and then loaded into the ODT. Subsequently the atoms were pumped to $F = 1$ and stored in the ODT. The population of atoms in $F = 2$ was probed using single photons resonant to $F = 2 \rightarrow F = 3$ of the D_2-line. The photons were detected with `Laser Components Count` single photon counters.

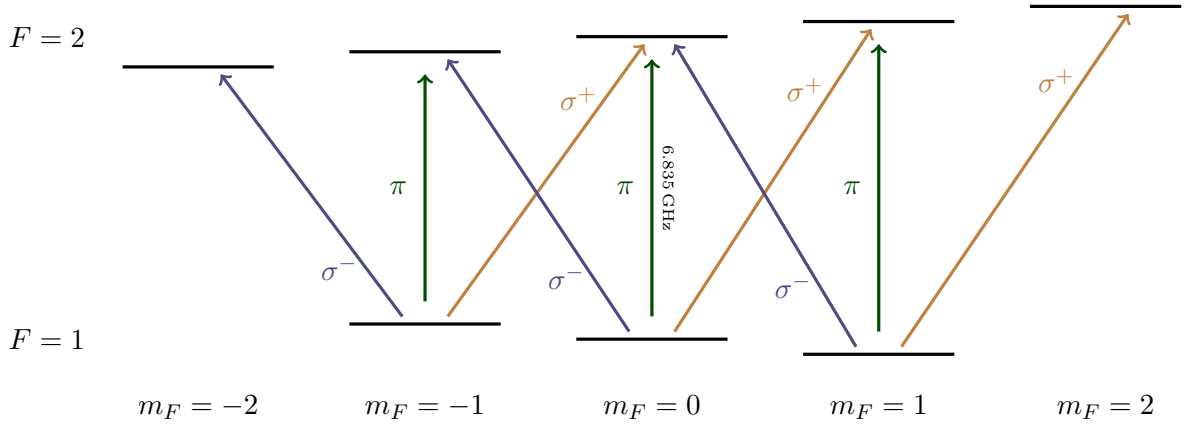

Fig. 10: Level scheme of a F=1 → F'=2 transition. The transition is driven by unpolarized microwave radiation. The levels are shifted due to the linear Zeeman effect by a magnetic field along the positive quantization axis. The two hyperfine levels have a different g-factor and therefore split in opposite directions. The individual transitions split different, therefore a variety of absorption features was observed. The $m_F = 0 \rightarrow m'_F = 0$ does not shift with magnetic field and is a suitable starting point while looking for the first signal.

The transition between the $F = 1$ and $F = 2$ hyperfine states was driven by a `Anritsu MG3962C` signal generator attached to a microwave antenna. The variety of possible transition of a Zeeman shifted transition is depicted in Fig. 10 The nullification was done such that the microwave frequency was swept around 6.835 GHz and if the microwave gets absorbed it drives atoms to $F = 2$. This population is then probed by the probe photons. The polarization is not well defined since the magnetic field's orientation is not known, therefore the in frequency outermost transition corresponds to the most sensitive transition regarding the magnetic field strength. The transition $F = 1 \rightarrow F = 2$ has a very small transition probability therefore the time in which the microwave is on has to be timed very precisely. This time is initially guessed and later determined by time resolved population measurements resulting in Rabi oscillations. The result is depicted in Fig. 11, the fit used was $f(t) = U_0 \sin^2(\Omega t) \exp(-t/\tau)$.

The procedure to find the currents through the coils at which the magnetic field was as low as possible was such that one transition of the spectrum was resolved while the magnetic field in one direction was altered. This procedure was done for each direction - corresponding to two coils - iterative. A sample measurement is depicted in Fig. 11.

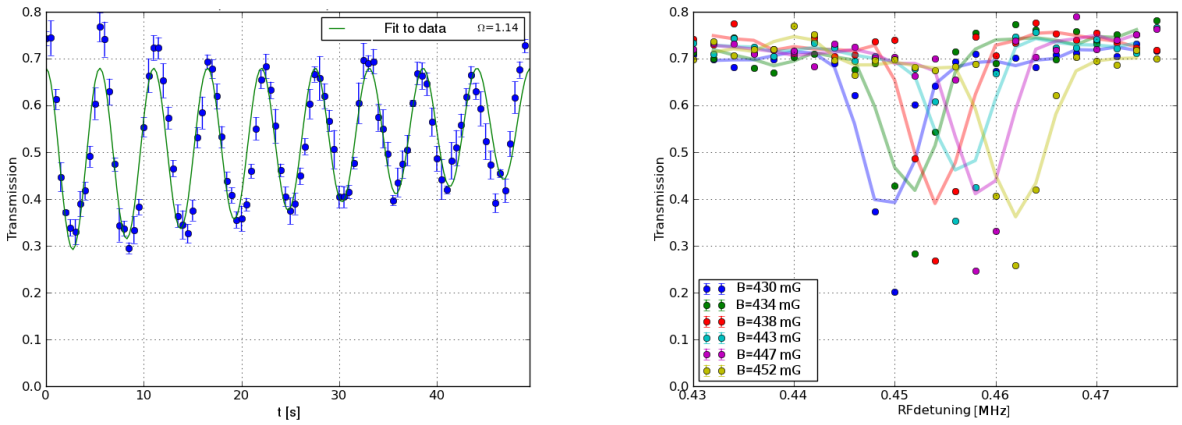

Fig. 11: Magnetic field nullification. (**Left**) Rabi oscillations between $F = 1$ and $F = 2$ driven by resonant radation. The resulting Rabi frequency obtained by a fit is $\Omega = 1.14 \cdot 10^3\,\mathrm{s}^{-1}$. The measurement was done sitting on the fewest shifted dip corresponding to a $m_F = 0 \rightarrow m'_F = 1$ transition. (**Right**) Absorption dips for different magnetic field settings. The dip probably corresponds to a $m_F = 0 \rightarrow m'_F = 1$ transition as it is the fewest shifted dip. The detuning is relative to the hyperfine splitting between $F = 1$ and $F = 2$. The dips are all shifted to zero detuning as good as possible, this sample measurement was taken for the magnetic field along the y-axis.

The remaining magnetic field was on the order of $B_{res} = 12\,\mathrm{mG}$.

5.2. Polarization Stability

To estimate the polarization instabilities of the fibers in the setup the polarization stability of a polarization-maintaining fiber was tested with a separate setup. The setup consisted of a rotation mounted polarizing beamsplitter in front of a fiber collimator aligned such that the axis of the beamsplitter and fiber coincide as good as possible and another rotation mounted cube behind the fiber was used to detect the fluctuations of the unwanted polarization component. The cube behind the fiber had its transmission axis perpendicular to the polarization coming out of the polarization-maintaining fiber. The cubes were used because they provide easy access to polarization extinction ratios of 10^{-3}. The powers are measured with power meters after the cube behind the fiber. The terms good and bad polarization refer to the polarization along the axis and perpendicular to the axis of the polarization-maintaining fiber. The polarization was measured over a timespan of several hours. The measurement depicted in Fig. 12 was taken when the conditions were probably nearly ideal since the temperature was very stable and no mechanical stress was applied through vibrations. The polarization extinction ratio is here calculated as good polarization divided by bad polarization, e.g. if the wanted or good polarization had power P_g and the other part power P_b, it would read

$$PER = 10 \log_{10} \left(\frac{P_g}{P_b} \right). \tag{72}$$

The polarizing beam splitter e.g. has a power extinction ratio of $-30\,\mathrm{dB}$, therefore the maximum extinction behind the fiber could only be that value. In Fig. 12 effects of the cube itself, e.g. the different transmission and reflection coefficients, are not respected. The cube in the rotational mount in front of the fiber was aligned by moderate heating of the fiber and subsequent reduction of the oscillations observed, similar to those in Fig. 12.

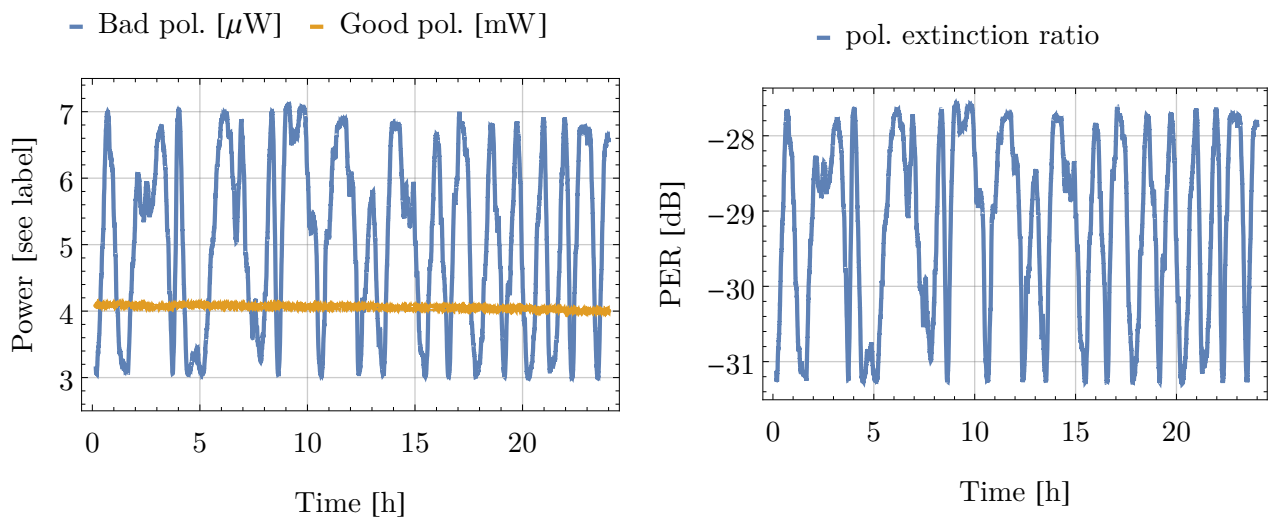

Fig. 12: Polarization stability measured 25.05.2015. (**Left**) Powers of the two polarization components. The two polarization components are measured individually, the decreasing over all power can maybe be explained by a change of the fiber coupling efficiency. (**Right**) Polarization extinction ratio. The polarization is not as stable as the cube is. The oscillations probably appear due to thermal effects, as this is also the effect occuring while heating and aligning the fiber.

5.3. Aligning the Raman Lattice Beams

The laser beams creating the optical potential should be overlapped with the atoms after previous cooling steps as good as possible in order to load the atoms into the global minimum of the lattice.

The lattice beams were initially adjusted using the steady state mode, as it was done in [Fölling, 2003]. The atoms are prepared in $F = 2$ after the magneto-optical trapping, it is therefore possible to shoot the steady state captured atoms away, if the laser is locked to the $F = 2 \rightarrow F = 2$ transition. Since the atoms are compressed after molasses the position of the atoms changed and the alignment had to be optimized. Further optimization was done such that all but one lattice beam were blocked, the atoms were prepared as already stated in $F = 2$ also after compression and molasses. After that part of the sequence a short pulse of lattice light was used to transfer atoms to $F = 1$, these atoms are not detected by the absorption imaging. In this manner each beam is aligned such that the absorption is as low as possible or that the lattice beam is overlapped. The retroreflected lattice beam is aligned in the same manner but with less power and shorter pulses since the cloud is hit twice.

The same procedure was conducted when we tried to implement the Raman sideband cooling inside the dipole trap. This was done since the Raman sideband cooling will in the end be conducted with atoms confined in the dipole trap.

5.4. Adiabatic Release and Capture

The atoms should be loaded into the optical lattice with as low heating as possible, the same is true for the release after the cooling sequence. To provide low heating adiabatic release and capture is necessary. If the lattice depth, which is proportional to the local intensity, is ramped up or down according to

$$I(t) = I_0 \frac{1}{(1 + \frac{t}{\tau})^2} \tag{73}$$

the atoms should not heat up as they are released from the lattice after cooling [Kerman *et al.*, 2000; Kastberg *et al.*, 1995]. The time constant τ is also suggested in [Kerman *et al.*, 2000] is chosen to be $100\,\mu$s. The ramp is provided by a `Agilent 33522A` function generator, since the stabilization is implemented using a logarithmic photodiode the reference signal has to follow the same behavior in order to realize the function. The ramp produced by the reference, measured by a liner photodiode and measured by the logarithmic photodiode is depicted in Fig. 13, a fit was conducted for the ramp measured by each element. Additionally the error signal while stabilizing the intensity is depicted.

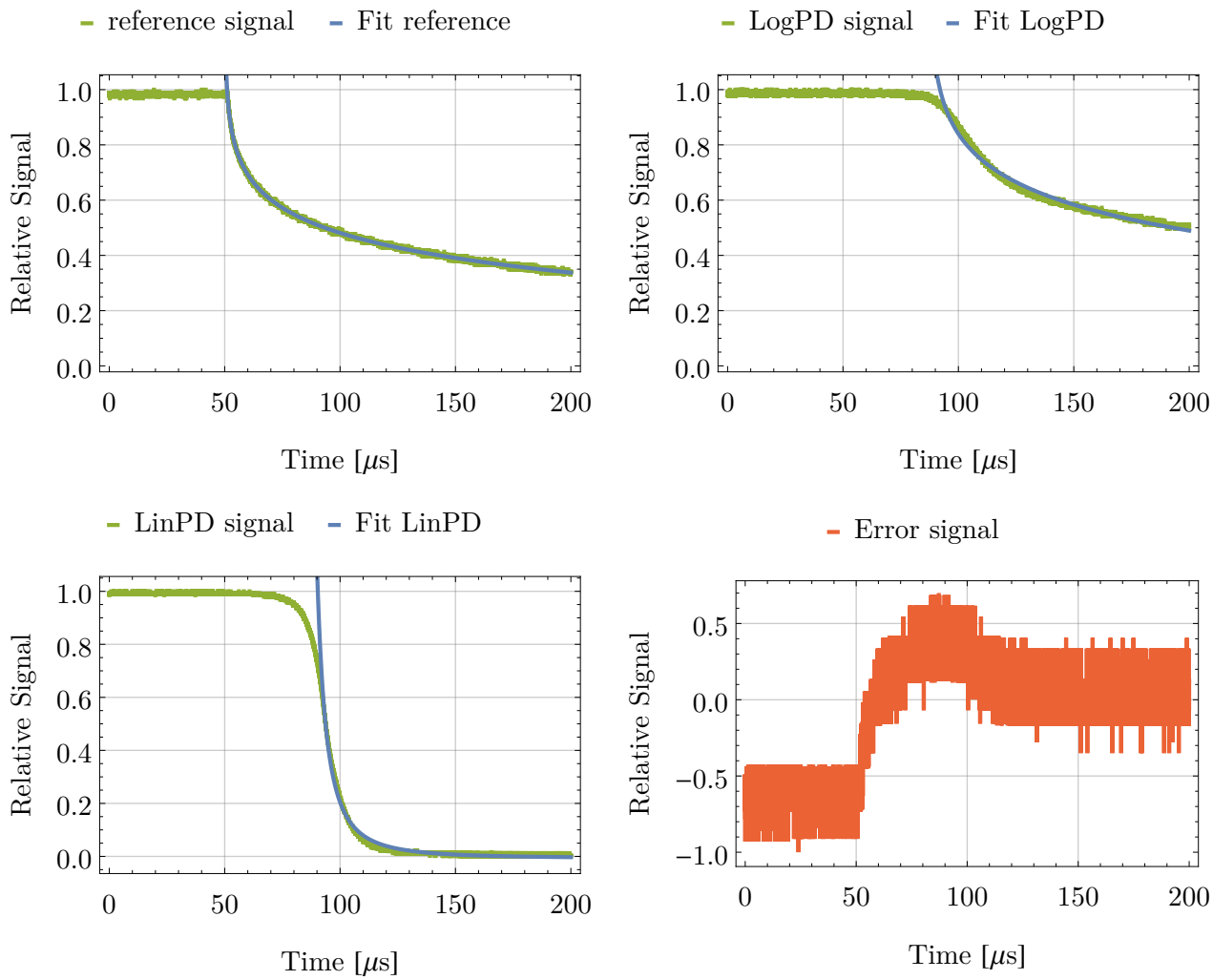

Fig. 13: Intensity ramp after Raman sideband cooling. The signal is normalized to the maximum signal. (**Top Left**) Signal provided by the function generator as reference signal. A fit with $\tau = 100\,\mu$s is also depicted to show whether it coincides. (**Top Right**) Signal after intensity stabilization measured with the logarithmic photodiode, same fit. (**Bottom Left**) Signal measured with a linear photodiode (linPD), same fit. (**Bottom Right**) Error signal provided by the PID-controller. The errorsignal in the beginning is there since this sequence was measured with insufficient power provided by the input to the AOM.

The fit function for the logarithmic signals reads

$$f_{\log}(t) = a \log(1 + \frac{t - t_0}{\tau}) + b, \tag{74}$$

Tab. 2: Resulting fit parameters for functions depicted in Fig. 13

	a [a.u.]	b [a.u.]	t_0 [μs]
Reference	0.13	0.39	150
LinPD	$6.75 \cdot 10^{-3}$	$-7.77 \cdot 10^{-3}$	182
Logarithmic PD	-0.16	0.51	187

whereas the function to fit to the linear photodiode's signal was

$$f_{lin}(t) = a\frac{1}{(1+\frac{t}{\tau})^2} + b. \tag{75}$$

The results for the fit parameters are listed in Tab. 2.

5.5. Testing the Raman Sideband Cooling

Cooling the atomic sample which is prepared in the lattice requires all parameters to be matched perfectly. One critical parameter is the magnetic field in order to lift the motional sidebands to degeneracy, directly associated with the magnetic field is the polarization of the Raman-pump beam. The pump beam enables this cooling technique since only atoms which are cycled have the possibility to lower their motional quantum number n.

As a first step the polarization of the Raman-pump beam was set to be purely σ^+ polarized for a magnetic field pointing along the z-axes. The cooling cycle would not work perfectly since the last quantum could not be removed in some cases (cf. section 3). At first we adapted the polarization settings of [Fölling, 2003], the resulting lattice is similar to the one presented in subsection 4.2, the only difference is that the vertical running beam is polarized in y-direction. As a first approach the magnetic field along all three directions was scanned. The sequence followed in all approaches is schematically depicted in Fig. 14. The term MOT-phase corresponds to the whole procedure related to the magneto-optical trapping, e.g. also optical molasses and compression.

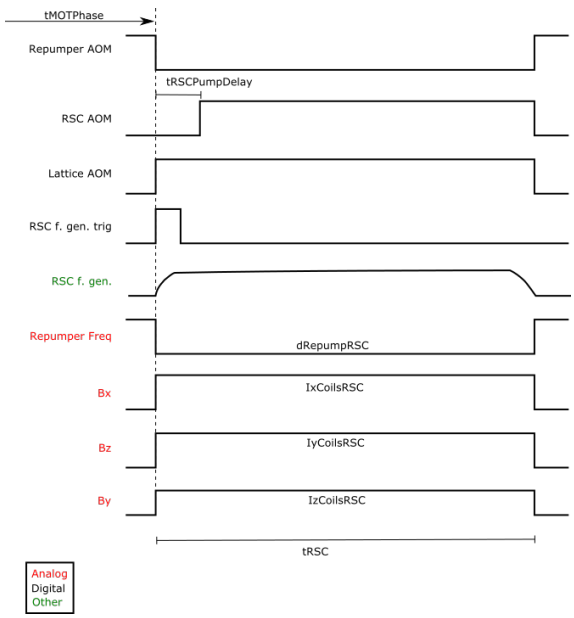

Fig. 14: Temporal sequence for Raman sideband cooling. After the MOT-phase the atoms are loaded into the lattice and the magnetic fields are applied simultaneously. The lattice is ramped up by the function generator which gets a trigger pulse. The length of the cooling cycle is sent to the function generator beforehand, therefore it is only triggered once. The Raman-pump beam is switched on with little delay.

To see whether the atoms get cooled or not, they get Raman sideband cooled for 20 ms with 1 ms time of flight afterwards. After this time the atoms remaining from the MOT-phase have disappeared and only atoms which are retained in the lattice are visible to the absorption imaging. In this first approach the magnetic fields were scanned as follows $B_x = 0:0{,}2:1{,}1\,\mathrm{G}; B_y = 0:0{,}4:2{,}2\,\mathrm{G}; B_z = 0:0{,}4:2{,}2\,\mathrm{G}$ (start:step:stop). The oscillation frequencies resulting from the input power of 20 mW expressed in form of the magnetic field necessary to lift the magnetic hyperfine levels to degeneracy were $B_{osc} = 0.3\,\mathrm{mG}$ along the strongly confining and $B_{osc} = 0.1\,\mathrm{mG}$ along the less confining axes. The lattice light was shut off immediately without ramping it down since we were not aiming for minimal temperature but seeing an effect of cooling. No matter which magnetic field settings were applied, no atoms could be retained.

Since the required magnetic fields are on the same order as the earth's magnetic field $B_{earth} \approx 0.5\,\mathrm{G}$ [Finlay *et al.*, 2010], the magnetic field was canceled out as good as possible (cf. subsection 5.1). Having (almost) no residual magnetic field the cooling should only depend on the magnetic field in z-direction. The magnetic field in z-direction was tested in finer steps, also both signs and therefore also both polarizations of the Raman-pump beam were tested, but still no atoms could be retained.

The magnetic field was then set to the theoretical value and the Raman-pump detuning was scanned. Raman cooling was done for 5 ms with 1 ms additional time of flight. An effect was observed and the temperature with and without Raman sideband cooling was measured. The Raman-pump detuning exhibits a dip in the cloud widths corresponding to lower temperatures, the scan is depicted in Fig. 15.

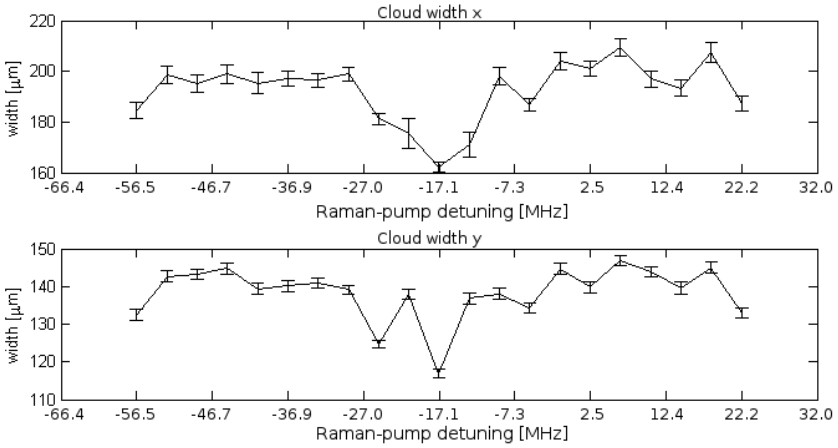

MHz.png

Fig. 15: Scan of the Raman pump detuning. The detuning is scanned around the resonance. A dip is observed, at that setting a temperature measurement is conducted to see whether this effect results from the cooling sequence Fig. 16.

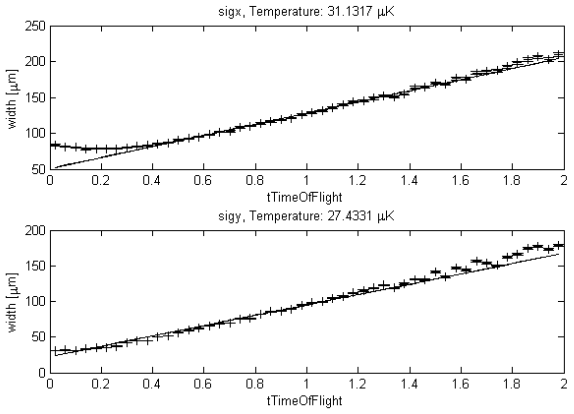

Temperature measurement **without** cooling.

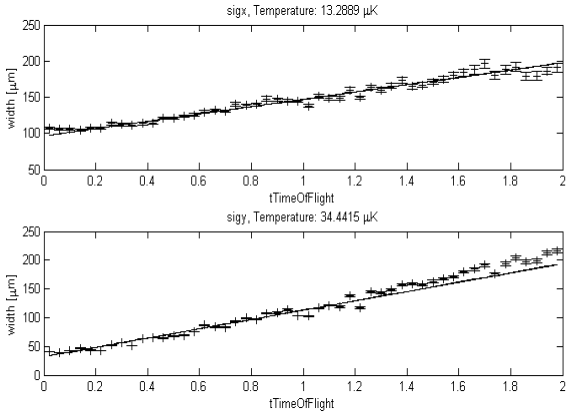

Temperature measurement **with** cooling.

Fig. 16: Time of flight sequence to determine the temperature. The cloud is initially smaller without Raman sideband cooling. The temperature in the imaging's $0x$-direction seems to be smaller if the sample gets cooled.

The Raman sideband cooling seems to have some effect Fig. 16 at the given detuning. The same measurements were conducted one day later but the results could not be reproduced.

After changing the polarization settings according to [Flir, 2006], the same measurements were conducted again. The polarization of the reflected beams is rotated by 90 ° after reflection so that the incoming beam is horizontally, the outgoing beam vertically polarized. The two running wave are polarized along each others wave vector. The same scans did not lead to clear signal of cooling nor heating.

Since it could be that if the degeneracy is not fulfilled for all three directions the cooling doesn't work, Raman sideband cooling in a one dimensional lattice was tested. To create this one dimensional lattice the two running waves were blocked and the reflected beam was reflected with identical polarization. The Raman-pump beam was applied while the lattice loaded ($t_{\mathrm{RSCpumpdelay}} = 0$ in Fig. 14) the atoms were heated or pushed out of the observation area of the imaging. This effect was affected by the magnetic strength in z-direction. Different Raman-pump powers didn't seem to have an effect.

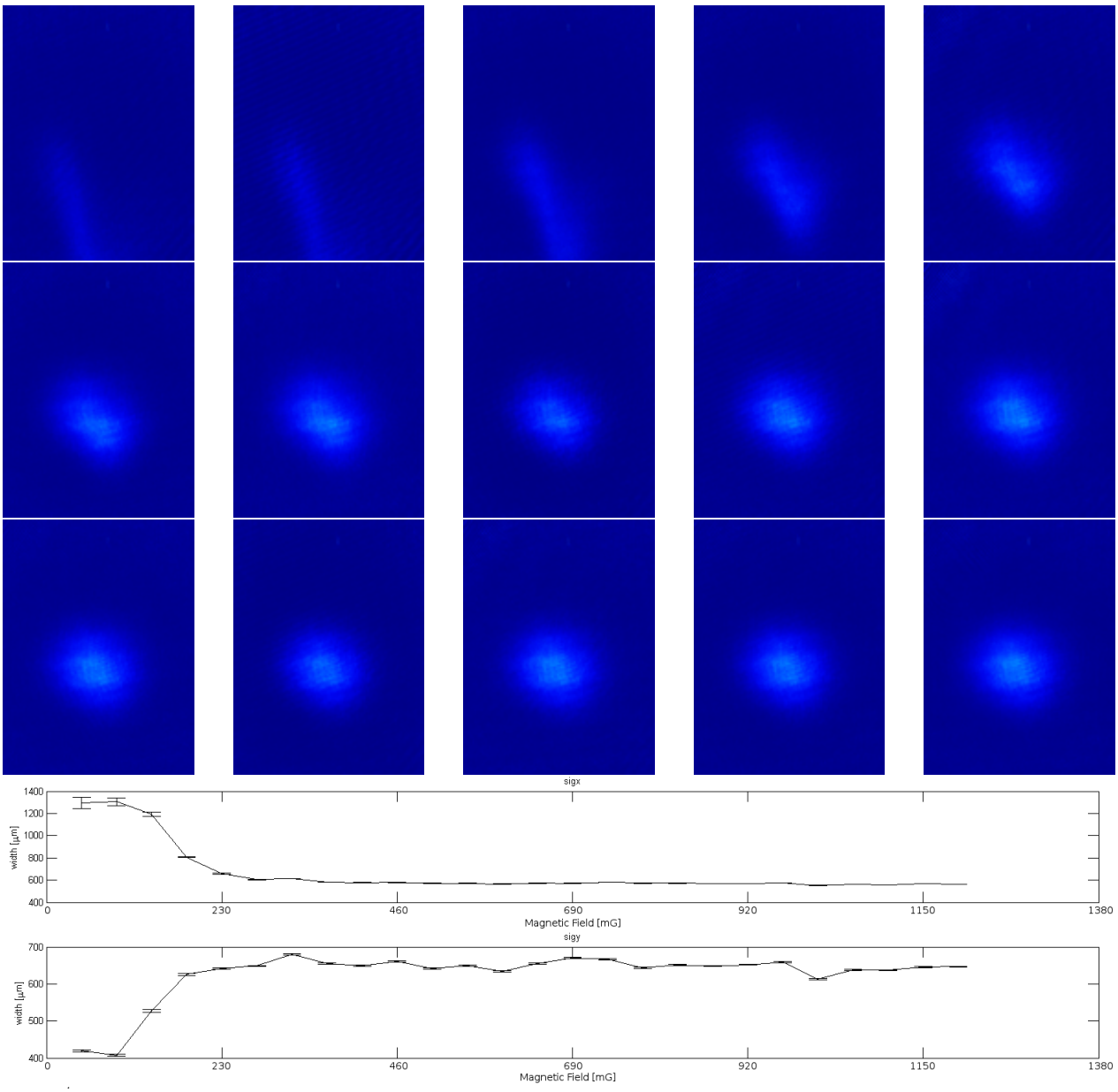

Fig. 17: Absorption images for increasing magnetic field in z-direction. The field increases from left to right and top to bottom from 0 mG with step size 46 mG. On the individual pictures the y-axis is mapped from right to left, the z-axis from top to bottom. The cloud widths corresponding to each image are depicted below, whether these results are reliable is questionable since the atom cloud does leave the section covered by the imaging system. The widths correspond to the widths on the images above.

6. Conclusion and Outlook

In this thesis the basic principles of Raman sideband cooling have been discussed. The elementary characteristics of the optical lattice potential have been calculated. The first trial-and-error measurements have so far not been fruitful, still some dependence on the magnetic field strength has been observed in a one dimensional lattice potential.

Since the cooling does not work yet one goal will certainly be to get the whole setup working.

Nevertheless a setup in principle able to cool a sample of atoms to temperatures of $\approx 1\,\mu$k has been implemented. The time needed to cool should be on the scale of milliseconds [Fölling, 2003; Kerman *et al.*, 2000]. One key element, the Raman pump beam, maybe was chosen to have to much intensity introducing heating which exceeded the possible cooling rates. The provided cooling should in principle be good enough to compensate for the scattering from the lattice. In connection with the overall setup which is used for quantum optical experiments it will be interesting to see differences in performance between Raman sideband cooling after the MOT-phase and cooling inside the optical dipole trap. Furthermore it would be interesting to measure the trap-depth and oscillation frequencies of the lattice and compare these to the values presented here.

A. PID

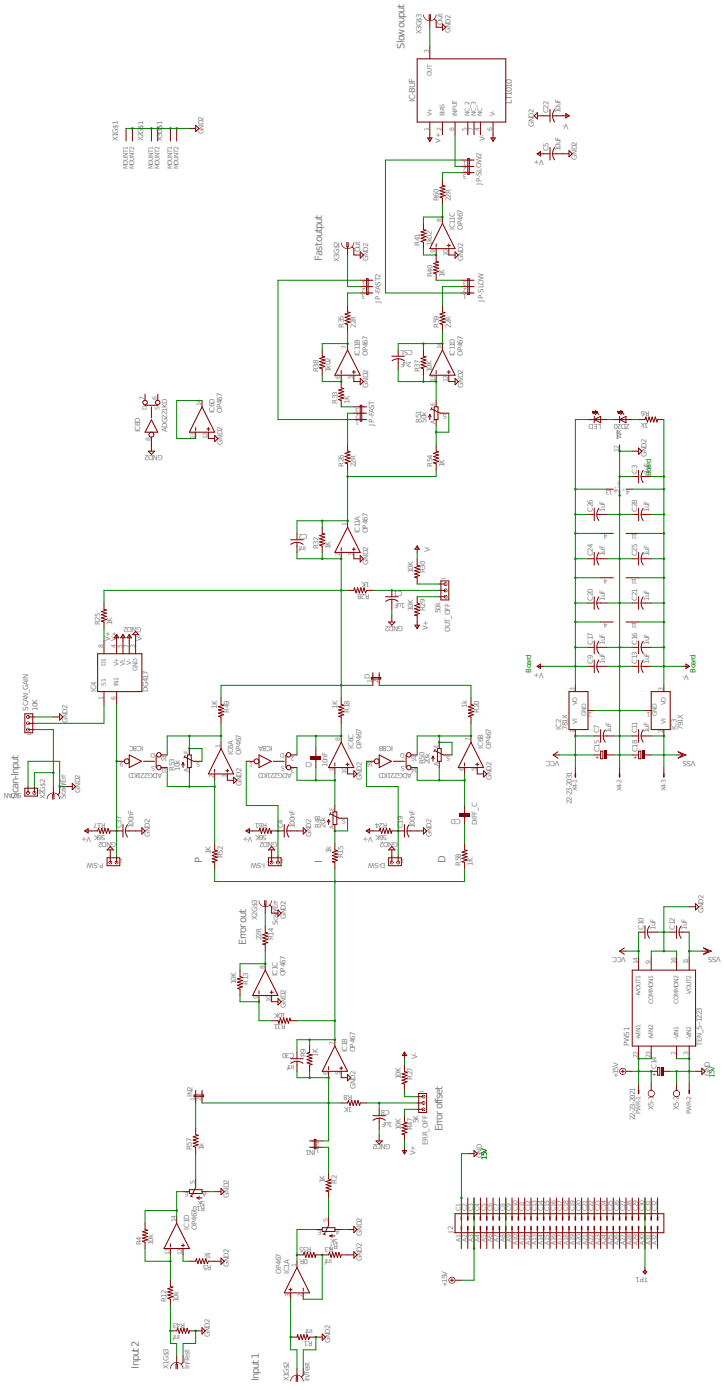

Fig. 18: Schematic of the internal electronis used to realize a PID-controller. Developed by Sebastian Hofferberth, Stephan Jannewein, Michael Schlagmüller and Kim Kafenda.

B. Matrices of the Polarizability Tensor

Another form of Equ. 35 would be

$$\hat{U} = E_L \vec{r}^* \hat{\alpha} E_L \vec{r}. \tag{76}$$

The polarizability $\hat{\alpha}$ can be expressed as a matrix $M_{\sigma,\sigma'}$ multiplied by a constant factor $\tilde{\alpha}$, this factor reads

$$\tilde{\alpha} = \frac{\left|\langle J \| \hat{\vec{d}} \| J' \rangle\right|^2}{\hbar \Delta}. \tag{77}$$

The matrices are composed of the $F = 1$ states, to avoid ambiguity the matrix and its components are stated,

$$|F = 1, m_F\rangle \langle F = 1, m'_F| = \begin{pmatrix} m_F = -1, m'_F = -1 & m_F = -1, m'_F = 0 & m_F = -1, m'_F = 1 \\ m_F = 0, m'_F = -1 & m_F = 0, m'_F = 0 & m_F = 0, m'_F = 1 \\ m_F = 1, m'_F = -1 & m_F = 1, m'_F = 0 & m_F = 1, m'_F = 1 \end{pmatrix} \tag{78}$$

$$M_{\sigma^+,\sigma^+} = \begin{pmatrix} 5/12 & 0 & 0 \\ 0 & 1/3 & 0 \\ 0 & 0 & 1/4 \end{pmatrix} \tag{79}$$

$$M_{\sigma^-,\sigma^-} = \begin{pmatrix} 1/4 & 0 & 0 \\ 0 & 1/3 & 0 \\ 0 & 0 & 5/12 \end{pmatrix} \tag{80}$$

$$M_{\pi,\pi} = \begin{pmatrix} 1/3 & 0 & 0 \\ 0 & 1/3 & 0 \\ 0 & 0 & 1/3 \end{pmatrix} \tag{81}$$

$$M_{\sigma^+,\pi} = \begin{pmatrix} 0 & 1/12 & 0 \\ 0 & 0 & 1/12 \\ 0 & 0 & 0 \end{pmatrix} \tag{82}$$

$$M_{\pi,\sigma^+} = \begin{pmatrix} 0 & 0 & 0 \\ 1/12 & 0 & 0 \\ 0 & 1/12 & 0 \end{pmatrix} \tag{83}$$

$$M_{\pi,\sigma^+} = \begin{pmatrix} 0 & 1/12 & 0 \\ 0 & 0 & 1/12 \\ 0 & 0 & 0 \end{pmatrix} \tag{84}$$

$$M_{\sigma^-,\pi} = \begin{pmatrix} 0 & 0 & 0 \\ 1/12 & 0 & 0 \\ 0 & 1/12 & 0 \end{pmatrix} \tag{85}$$

$$M_{\sigma^+,\sigma^-} = M_{\sigma^-,\sigma^+} = \begin{pmatrix} 0 & 0 & 0 \\ 0 & 0 & 0 \\ 0 & 0 & 0 \end{pmatrix} \tag{86}$$

C. References

Appel, J., A. MacRae, and A. I. Lvovsky (2009), Measurement Science and Technology **20** (5), 055302.

Bloch, F. (1929), Zeitschrift für Physik **52** (7-8), 555.

Boyd, R. W. (2008), *Nonlinear Optics (Third Edition)*, third edition ed. (Academic Press, Burlington).

Vuletić, V., C. Chin, A. J. Kerman, and S. Chu (1998), Phys. Rev. Lett. **81**, 5768.

Cline, R. A., J. D. Miller, M. R. Matthews, and D. J. Heinzen (1994), Opt. Lett. **19** (3), 207.

Cohen-Tannoudji, C., J. Dupont-Roc, and G. Grynberg (2004), *Atom-photon interactions: basic processes and applications* (Wiley-VCH, Weinheim).

Deutsch, I. H., and P. S. Jessen (1998), Phys. Rev. A **57**, 1972.

Edmonds, A. R. (1957), *Angular momentum in quantum mechanics*, Investigations in physics ; 4 (Princeton Univ. Pr., Princeton, NJ).

Eschner, J., G. Morigi, F. Schmidt-Kaler, and R. Blatt (2003), J. Opt. Soc. Am. B **20** (5), 1003.

Finlay, C. C., S. Maus, C. D. Beggan, T. N. Bondar, A. Chambodut, T. A. Chernova, A. Chulliat, V. P. Golovkov, B. Hamilton, M. Hamoudi, R. Holme, G. Hulot, W. Kuang, B. Langlais, V. Lesur, F. J. Lowes, H. Lühr, S. Macmillan, M. Mandea, S. McLean, C. Manoj, M. Menvielle, I. Michaelis, N. Olsen, J. Rauberg, M. Rother, T. J. Sabaka, A. Tangborn, L. Tøffner-Clausen, E. Thébault, A. W. P. Thomson, I. Wardinski, Z. Wei, and T. I. Zvereva (2010), Geophysical Journal International **183** (3), 1216.

Flir, A. (2006), *Implementierung und Untersuchung von Raman-Seitenbandkühlung zur Erzeugung eines ultrakalten Cäsiumgases*, Master's thesis (Universität Innsbruck).

Fölling, S. (2003), *3D Raman sideband cooling of rubidium*, Master's thesis (Universität Heidelberg).

Foot, C. J. (2005), *Atomic physics*, 1st ed. (Oxford University Press, Oxford).

Gerlach, W., and O. Stern (1922), Zeitschrift für Physik **9** (1), 349.

Grimm, R., M. Weidemüller, and Y. B. Ovchinnikov (2000) (Academic Press) pp. 95 – 170.

Hamann, S. E., D. L. Haycock, G. Klose, P. H. Pax, I. H. Deutsch, and P. S. Jessen (1998), Phys. Rev. Lett. **80**, 4149.

Jackson, J. D. (1982), *Klassische Elektrodynamik* (de Gruyter, Berlin; New York).

Kastberg, A., W. D. Phillips, S. L. Rolston, R. J. C. Spreeuw, and P. S. Jessen (1995), Phys. Rev. Lett. **74**, 1542.

Kerman, A. J., V. Vuletić, C. Chin, and S. Chu (2000), Phys. Rev. Lett. **84**, 439.

Scully, M. O., and M. S. Zubairy (1997), *Quantum optics*, 1st ed. (Cambridge University Press, Cambridge).

Steck, D. A. (2001), "Rubidium 87 d line data," Available online at `http://steck.us/alkalidata` (revision 2.1.4, 23 December 2010).

Steck, D. A. (2007), "Quantum and atom optics," Available online at `http://steck.us/teaching` (revision 0.10.1, 30 April 2015).

Tresp, C. (2013), *A Setup for Highly Precise Excitation and Detection of Rydberg Atoms*, Master's thesis (Universität Stuttgart).

Treutlein, P., K. Y. Chung, and S. Chu (2001), Phys. Rev. A **63**, 051401.

Wineland, D. J., C. Monroe, W. M. Itano, D. Leibfried, B. E. King, and D. M. Meekhof (1998), J. Research National Institute Standards Technology **103** (3), 259.